ROMA
TRE
UNIVERSITÀ DEGLI STUDI

Ph.D. in Civil Engineering

XXX Cycle

Ph.D. Thesis
Numerical simulation of axisymmetric three-dimensional gravity currents generated by lock-exchange

Ph.D. Student: Roberto Inghilesi

Claudia Adduce

Ph.D.Tutor: Prof. Claudia Adduce

Ph.D. Coordinator: Prof. Gianmarco de Felice

Collana delle tesi di Dottorato di Ricerca
in Ingegneria Civile
Università degli Studi Roma Tre
Tesi n°68

Numerical simulation of axisymmetric three-dimensional gravity currents generated by lock-exchange

Roberto Inghilesi

January 10, 2018

Abstract

The unconfined three-dimensional gravity current generated by lock-exchange using a small dividing gate in a sufficiently large tank is investigated through a series of large eddy simulations under the Boussinesq approximation. The study shows that, after an initial transient, the flow can be separated into an axisymmetric expansion and a globally translating motion. In particular, the circular frontline spreads like a constant flow-rate, axial symmetric gravity current about a virtual source translating along the symmetry axis. The flow is characterised by the presence of lobe and cleft instabilities and hydrodynamical shocks. Depending on the Grashof number, the shocks can either be isolated or produced continuously. In the latter case a typical ring structure is visible in the density and velocity fields. The analysis of the frontal spreading of the axisymmetric part of the current indicates the presence of three regimes, namely, a slumping phase, an inertial-buoyancy equilibrium regime and a viscous-buoyancy equilibrium regime. The viscous-boundary phase is well in accord with the model of Huppert [1982], while the inertial phase is consistent with the experiments of [Britter, 1979], conducted for purely axial symmetric, constant inflow, gravity currents. The adoption of the slumping model of Huppert and Simpson [1980], which is here extended to the case of constant-flow-rate cylindrical currents, allows reconciling different theories about the initial radial spreading in the context of different asymptotical regimes. As expected, the slumping phase is governed by the Froude number at the lock's gate, whereas the transition to the viscous phase depends on both the Froude number at the gate and the Grashof number. The identification of the inertial-buoyancy regime in the presence of hydrodynamical shocks for this class of flows is important, due to the lack of analytical solutions for the similarity problem in the framework of shallow water theory. This fact has considerably slowed the research on variable-flow-rate axisymmetric gravity currents, as opposed to the rapid development of the knowledge about cylindrical constant volume and planar gravity currents, despite their great environmental relevance.

The results are relevant for the assessment of many environmental processes, among which the near-field spreading of riverine freshwater in coastal waters and the dispersion associated with severe cases of oil spill at sea.

Contents

0.1 Introduction xv

I Methodology 1

1 Axial symmetric gravity currents with variable inflow 3

2 Problem description 7
  2.1 Numerical formulation 7
  2.2 Numerical implementation 9
  2.3 Test cases 12

II Results 15

3 Axial symmetry 17

4 Rings 23
  4.1 Low Grashof number 23
  4.2 High Grashof number 28
  4.3 The reverse current 39

5 Spreading regimes for axisymmetric, constant volume flow gravity currents 43
  5.1 Dimensional analysis and asymptotic solutions 43
  5.2 Evaluation of the regimes 46
  5.3 Slumping phase 51
  5.4 Inertial-buoyancy equilibrium phase 51
  5.5 Viscous-buoyancy equilibrium phase 57

III Conclusions 61

List of Figures

1.1 Operation Crossroads ‘Baker experiment’– base surge formed by nuclear submarine explosion 3
1.2 base surge generated by volcanic explosion 4
1.3 Deepwater Horizon rig in flames, 2010 5
1.4 Deepwater Horizon oil spill, SAR image over Louisiana 2010 . 5
1.5 25 June 2006, severe convection over Austria: images from Meteosat MSG2; EUMETSAT training Library 6
1.6 Thermal scanning of Lake Michigan, 1973, from ‘Application of remote sensing to the investigation of nearshore mixing and coastal entrapment in large water bodies’, Theodore Green IIIa and Robert A. Ragotzkie, in A Progress Report On Multidisciplinary Research On The Application Of Remote Sensing To Water Resources Problems, 1972-1973, NATIONAL AERONAUTICS AND SPACE ADMINISTRATION, Office of University Affairs Washington, D.C. 20546 6

2.1 Sketch of the lock-release tank: (a) top view and (b) side view. 10
2.2 Nondimensional volume flow vs. Gr 14

3.1 Density field on the midplane $y = y_0$, $t = 8.7$, case S11 . . . 18
3.2 Case S2 $Gr = 5.0 \cdot 10^5$, $\epsilon = 0.03$; frontline $G(x, y)$ at t=32 . 19
3.3 Case S2: $Gr = 5.0 \cdot 10^4$, $\epsilon = 0.03$; top panel: $\frac{a^2}{b^2}$ vs. t; bottom panel: $x_c(t)$ vs. t 20
3.4 Case S13: $Gr = 5.3 \cdot 10^8$, $\epsilon = 0.02$; top panel: $\frac{a^2}{b^2}$ vs. t; bottom panel: $x_c(t)$ and $R(t)$ vs. time 21
3.5 Case S12 (experiment) evolution in time of the frontline at $t = 2.8, 5.7, 8.6, 11.5, 14.4$, and 17.3; grey area is the planform of the gravity current; black line: circle centred at the centre of the separating gate and radius equal to the distance from the gate to the frontline on the x axis; blue lines: circles centred at x_c and radius $R_b = R_a$; asterisks: position of the centre (x_c, y_0) and of the upper extremal (x_c, y_+) 22

4.1 Hovmoller diagram, case S1, simulation $Gr = 8.1 \cdot 10^4$ 24

4.2 Density isosurface at $\rho = 3\%$, case S3, $t = 8.7$ 24

4.3 Density isosurface at $\rho = 3\%$ and velocity field on the mid plane (x, z), case S3, $t = 8.7$ 25

4.4 top: non dimensional radial velocity $\frac{|\bar{u}|}{U_l}$ on the mid-plane $y = y_0$; the continuous black line indicates the depth $h_l = \frac{\overline{g'h}}{g'}$ and the broken black line marks h_t, i.e. the interface $\rho = 3\%$, bottom: Froude number Fr_H vs. x. Case S3, $t = 8.7$ 26

4.5 top: non dimensional radial velocity $\frac{|\bar{u}|}{U_l}$ on the mid-plane $y = y_0$; the continuos thick black line indicates the depth $h_l = \frac{\overline{g'h}}{g'}$ and the broken black line marks h_t, i.e. the interface $\rho = 3\%$, bottom: Froude number Fr_H vs. x. Case S3, $t = 16.$ 27

4.6 Hovmoller diagram, case S3, simulation $Gr = 2.0 \cdot 10^6$ 28

4.7 Density field on the horizontal plane at $z = 0.1$, $t = 8.7$, case S11 29

4.8 Top view image of the experiment S12, $t = 14.5$ 30

4.9 Case S11: $\rho = 3\%$ isosurface, $t = 8.7$ 31

4.10 Case S11: velocity field on the mid-plane (x, z), $Gr = 8.1 \cdot 10^8$, $\epsilon = 0.03$, $t = 12$ 31

4.11 top: non dimensional velocity $\frac{|\bar{u}|}{U_l}$ on the mid-plane $y = y_0$; the thick black line indicates the depth $h_l = \frac{\sqrt{g'h}}{g'_0}$ and the thin line marks the interface $\rho = 3\%$; bottom: Froude number Fr_H vs. x ; case S11, $t = 8.7$ 32

4.12 top: non dimensional velocity $\frac{|\bar{u}|}{U_l}$ on the mid-plane $y = y_0$; the black continuous line indicates the depth $h_l = \frac{\sqrt{g'h}}{g'_0}$ and the black broken line marks the interface $\rho = 3\%$; bottom: Froude number Fr_H vs. x ; case S11, $t = 16.0$ 33

4.13 square of distance of the first ring from the symmetry axis (r_{1r}) with respect to the velocity times the travel time (t_{1r}) of the disturbance carried by the fastest gravity wave 35

4.14 Hovmoller diagram case S11, simulation $Gr = 8.1 \cdot 10^8$ 37

4.15 Hovmoller diagram case S13, simulation $Gr = 5.4 \cdot 10^8$ . . . 37

4.16 Case S13: $\rho(x, y, z_c)$, $t = 64$, case S13 38

4.17 Dimensionless frequency of ring generation η vs. Gr; dots represent S6-S11; cross is S13; dashed line indicates $\bar{\eta}$ 38

4.18 ρ on the meridian plane at $y = y_0$, $t = 8.2$, case S10 39

4.19 ρ on the horizontal plane at $z = H - 0.2$, $t = 8.2$, case S10 . . 40

4.20 ρ on the meridian plane at $y = y_0$, $t = 13.5$, case S10 41

4.21 ρ on the horizontal plane at $z = H - 0.2$, $t = 13.5$, case S11 . 42

5.1 Non-dimensional front position vs. non-dimensional time. The vertical dashed line at $t/t_v = 1$ represents the transition to the viscous phase. Cases S1–S5: low Grashof number 48

5.2 Non-dimensional front position vs. non-dimensional time cases S6÷S11: high Grashof number; red dots are experimental data from S12 49
5.3 Case S13 extended domain ED; non-dimensional front position vs. non-dimensional time. The vertical dashed line at $t/t_v = 1$ represents the transition to the viscous phase. High-frequency oscillations at $t/t_v > 1$ are a border effect. 50
5.4 Domain of existence of the slumping regime (5.11), non-dimensional radial position vs. non-dimensional time. Vertical dashed line indicates the expected transition from the slumping phase to the inertial phase 52
5.5 Non-dimensional coefficient b_f normalised by C_{sl} (5.11) vs. Gr, cases S1–S11. Dashed line represents $\bar{\mu} =< \frac{b_f}{C_{sl}} >$ 53
5.6 Domain of existence of the inertial-buoyancy regime (5.12): non-dimensional radius vs. non-dimensional time. Dashed line indicates $R/(c_f + d_f t^{3/4}) = \kappa_s$; dotted lines indicate the interval at the 95 % confidence level. Vertical dash-dot line indicates the theoretical transition to the inertial regime . . . 54
5.7 Non-dimensional coefficient $\delta = \frac{d_f}{C_{in}}$ in (5.12) vs. Gr, cases S3–S12. Dashed line represents $\bar{\delta} =< \frac{d_f}{C_{in}} >$ 55
5.8 Inertial buoyancy regime (5.6): non-dimensional radius vs. non-dimensional time scaled as in [Britter, 1979]. Dashed red line indicates $R/(C_{in}t^{3/4}) = \kappa_1$; dotted line indicates $R/(C_{in}t^{3/4}) = \kappa_2$. Dot-dashed line indicates $R/(C_{in}t^{3/4}) = \kappa_3$. Vertical dash-dot line indicates the theoretical transition to the inertial regime; Q is assumed as the flow rate in the axial position 56
5.9 Temporal domain of existence of the viscous-buoyancy regime (5.13): non-dimensional radial position vs. non-dimensional time. Dotted line indicates $\frac{R_3}{e_f + g_f\sqrt{t}} = 1$. 58
5.10 Distribution of the non-dimensional coefficient λ in the fit (5.13) vs. Gr, cases S1–S4. Dotted line represents $\bar{\lambda} =< \frac{g_f}{C_{vis}} >$ 59
A1 Case S5: $Gr = 8.1\cdot 10^6$, $\epsilon = 0.03$; top panel $\frac{a^2}{b^2}$ vs. t; bottom panel $x_c(t)$ vs. t 67
A2 Case S5 a) t=9.3, b) t=9.8, c) t=10.1, and d) t= 10.5; front-line $G(x, y)$ is indicated with black dots; C_a: blue dashed circle; C_b: red dot-dashed circle; C_f: black solid circle; y_+ and y_- are indicated with red crosses 68

List of Tables

2.1 Geometrical parameters for the laboratory domain (LD) and the extended domain (ED). 11

2.2 S1–S11: numerical simulations in the LD, S12: laboratory experiment in the LD, and S13: numerical simulation in the ED 13

4.1 R_r^2 square of distance of the first ring from the symmetry axis, t_r^2 time of propagation of the wave with velocity U_b 36

5.1 'Best' transition times and corresponding front positions estimated from the statistical evaluation of the time series. . . . 47

Nomenclature

$\bar{\delta}$	estimate of the mean value of the distribution of non-dimensional ratios $\delta = \frac{d_f}{C_{in}}$
$\bar{\lambda}$	estimate of the mean value of the distribution of non-dimensional ratios $\lambda = \frac{g_f}{C_{vis}}$
$\bar{\mu}$	estimate of the mean value of the distribution of non-dimensional ratios $\mu = \frac{b_f}{C_{sl}}$
$\bar{\rho}$	filtered dimensionless residual density
Δx_i^+	Cartesian non dimensional grid cell dimension in wall units
δ_{ij}	Kronecker delta tensor
$\dot{x}(t)_f$	translating velocity of the axis of symmetry
ϵ	fractional density difference $\frac{\Delta\rho}{\rho_0}$
κ	universal parameter in the spreading law for inertial-buoyancy regime, $\kappa = \kappa_s \bar{\delta}$
κ_s	constant coefficient for the spreading law in the inertial-buoyancy regime
λ_j	sub-grid-scale mass flux
$\langle\rho\rangle$	constant term in Boussinesq expansion of the density field [kg/m^3]
ν	kinematic viscosity [m^2/s]
ψ	threshold level in density
$\rho'(x_i, t)$	residual term in Boussinesq expansion of density field [kg/m^3]
ρ_0	reference density [kg/m^3]
ρ_1	density of the fluid in the lock at the beginning of the simulation/experiment [kg/m^3]

ρ_2	density of the fluid in the tank at the beginning of the simulation/experiment [kg/m^3]
ρ_{tot}	density field [kg/m^3]
τ_{ij}	sub-grid-scale momentum flux
$\tilde{\rho}$	leading term depending on x_3 in Boussinesq expansion of the density field [kg/m^3]
a	major axis of the ellipse formed by the frontline
a_f, b_f	regression coefficients in the slumping regime
b	minor axis of the ellipse formed by the frontline
c_f, d_f	regression coefficients in the inertial-buoyancy regime
C_{in}	inertial-buoyancy spreading coefficient
C_{sl}	slumping spreading coefficient
C_{vis}	viscous-buoyancy spreading coefficient, after Britter [1979]
e_f, g_f	regression coefficients in the viscous-buoyancy regime
$f_l(y)$	external frontline on the plane $z = z_b$ (explicit function)
Fr	Froude number
Fr_H	Froude number expressed as in [Shin et al., 2004],$Fr_H = \frac{\bar{u}_r}{\sqrt{\overline{g'h}}}$
g	acceleration of gravity [m/s^2]
g'	reduced gravity [m/s^2]
$G(x, y)$	external frontline on the plane $z = z_b$ (implicit function)
Gr	Grashof number
H	depth of the tank z-direction
h	depth of the gravity current
h_e	equivalent depth of the current [m]
h_l	depth of the core of the current,$h_l = \frac{\overline{g'h}}{g'_0}$, as in Shin et al. [2004] [m]
h_t	depth the current evaluated as the height of the $\rho = 3$ % isopycnal [m]

k	diffusivity of the saline solution [m^2/s]
L	length of the tank (x-direction)
L_s	length scale =H [m]
Q	volume flow rate of dense fluid at the separating gate [m^3/s]
R	radius of the axial symmetric current with respect to the axis of symmetry, obtained from the decomposition of a three-dimensional lock-exchange current
r	radius of a purely axial symmetric current
R'_i	radial position for transition to inertial-buoyancy regime, statistical procedure
R'_s	radial position for transition to slumping regime, statistical procedure
R_1	radial front position in the slumping part of the time series
R_2	radial front position in the inertial-buoyancy part of the time series
R_3	radial front position in the viscous-buoyancy part of the time series
R_a	radius of curvature of the frontline along the x direction
R_b	radius of curvature of the frontline along the y direction
R_{1r}	non dimensional radial distance from the axis of symmetry to the position of the hydraulic jump
r_{1r}	distance from the axis of symmetry to the position of the hydraulic jump [m]
Re	Reynolds number
Sc	Schmidt number $Sc = \nu/k$
t	time
t'_i	time for transition to inertial-buoyancy regime, statistical procedure
t'_s	time for transition to slumping phase, statistical procedure
t'_v	time for transition to viscous-buoyancy regime, statistical procedure
t_0	time after which Q becomes stationary
t_f	end time of simulation/experiment
t_i	time scale for transition to buoyancy-inertial regime

T_s	time scale $=\frac{H}{U_s}$ [s]
t_v	time scale for transition to buoyancy-viscous regime
t_{r1}	time of formation of the first ring [s]
t_r	non dimensional travel time of the fastest gravity wave [s]
U_b	buoyancy velocity [m/s]
U_f	front velocity
u_i	Cartesian coordinates velocity in tensorial notation, $i = 1, 2, 3$
U_l	local average buoyancy velocity $U_l = \sqrt{g'h}$, as in Shin et al. [2004] [m/s]
u_r, u_θ, u_z	velocity of the axial symmetric current in cylindrical coordinates r, θ, z
U_s	$\sqrt{g'H}$ velocity scale [m/s]
u_τ	friction velocity
x_0	lock length
x_c	position of the axis of symmetry of the current in the mid plane $y = y_0$
$x_c(t)$	position of the axis of symmetry on the mid plane $y = y_0$
x_f	position of the frontline in the mid plane $z = z_0$ with respect to the axis of symmetry of the current
x_i	Cartesian coordinates tensorial notation, $i = 1, 2, 3$
x_i^+	Cartesian non dimensional coordinates in wall units
y_0	half-width of the tank y-direction
z_b	minimum height at which the velocity profile is not significantly affected by the distance from the bottom
z_c	level on the vertical axis z at which the HD is calculated
u, v, w	velocity in cartesian coordinates, vector notation
x, y, z	Cartesian coordinates, vector notation

0.1 Introduction

Many natural and industrial flows at several spatial scales are driven by density gradients and are bounded only by a horizontal rigid surface. Despite the extensive range of scales involved, ranging from synoptic to laboratory scale, these flows are commonly known in fluid mechanics as gravity currents as opposed to wind-driven or the more complicated thermohaline currents. Many different cases that exhibit a planar or axial symmetric nature have been extensively described in the literature, The general subject is referred to the classical introduction of Simpson [1997] for an extensive presentation of the several possible manifestations of gravity currents in nature and in laboratory, and to Meiburg et al. [2015] for a comprehensive description of the methods and models used to describe them. Dai [2013] studied the properties of frontal dynamics and mixing in gravity currents propagating on inclined bottoms. Advanced numerical methods have been proposed to study planar gravity currents in complex geometries or bathymetries, e.g. Dai [2015], Gonzalez-Juez et al. [2010], Ooi et al. [2007, 2009], Ottolenghi et al. [2017], Tokyay et al. [2014]. Experimental studies on cylindrical currents in a rotating tank were recently discussed by Dai and Wu [2016]. A series of complex experiments of gravity currents in a rotating, wedge-shaped channel generated by a continuous inflow of a dense fluid were described in Cuthbertson et al. [2011, 2014].

When no clear symmetry is present in the flow, as is the case for the three-dimensional unconfined gravity current problem, references in the literature are few and sparse. Ross et al. [2002] studied the instantaneous release of a three-dimensional (3D) gravity current on an unconfined uniform slope. La Rocca et al. [2008, 2012] described a series of lock-exchange experiments of unbounded gravity currents generated in a large square tank. Prior to their study, Maxworthy [1980] had presented experiments on 3D gravity currents generating trains of solitary waves in a stratified environment realised in a similar large tank. The geometries of the two experimental set-ups differed in terms of the size of the volume of fluid in the lock, but despite the differences, it turns out that in many cases, the 3D gravity currents generated appeared to acquire a definite axial symmetry in a short time.

The recent experimental results of Lombardi et al. [2017], obtained in a set up similar to that used by La Rocca et al. [2008], show that the size of the lock width has a significant effect on the development of the gravity current not only in the evolution of the shape of the planform, but also in terms of the propagation speed of the frontline. For relatively large lock gates the current is similar to a planar current and develops a characteristic slumping regime with a constant front speed, while for lock gate widths under a definite threshold the current acquires a cylindrical symmetry and the spreading is always decelerating.

Typical large-scale axisymmetric gravity currents are produced in the ocean by buoyant columns of fluid hitting an inversion layer or the sea surface, as may occur with leaks in submerged oil pipes. When the volume of the released fluid is constant (and typically small in laboratory experiments), the radially spreading current generated at a point source has been successfully investigated analytically and numerically in the context of the shallow water approximation to reveal the characteristic regimes [Abbott and Hayashi, 1967, Hallworth et al., 2001, Huppert, 2006, Penney and Thornhill, 1952, Ungarish, 2009]. The radial flow is known to be affected by instabilities at the expanding frontline, and the numerical study of Cantero et al. [2007] provided a thorough investigation of the lobe and cleft instabilities, the three-dimensional vortex dynamics and the relation with the turbulent structures in the flow. In the case of a very large amount of release, as is the case with the experiments of Lombardi et al. [2017], the total volume of fluid generating the current is variable with time, and the generated currents are considerably more massive and faster. Even in the simplest case of constant inflow, there is relatively little confidence about the dynamics of axisymmetric gravity currents. In fact, for this type of flow, only the viscous-buoyancy equilibrium has been satisfactory described in the context of shallow water theory in the sense that similarity solutions [Huppert, 1982] match the observed spreading in the development of the axisymmetric gravity current [Britter, 1979, Didden and Maxworthy, 1982].

Similarity solutions are not available for the initial part of the spreading, i.e. in the inertial-buoyancy equilibrium. Britter [1979] was the first to investigate the inertial regime for negatively buoyant axisymmetric currents at a constant flow rate running on a rigid bottom in a laboratory. The experiments presented in his study were conducted using solutions of salt and water inside two long sector-shaped tanks filled with fresh water. During the tests, care was taken to avoid the introduction of mixing and radial momentum at the source. In fact, they produced an initial plane current at a constant flow rate, entering in the diverging sector only after stabilising. This procedure was necessary because, as reported by Grundy and Rottman [1986], in some of the sector-shaped tank experiments, multiple concentric rings were formed. The presence of large-scale regular structures in the temperature fields of axisymmetric density currents has been observed since the first use of thermal imagers in remote sensing. Alternating bands of warm-cold waters have been recorded in infrared images of thermal plumes in rivers [Garvine, 1984, Green and Ragotzkie, 1973] and in fjords [Simpson, 1997]. At smaller scales, periodic ring structures have also been observed in laboratory experiments with constant inflows and even in fixed-volume, axisymmetric gravity currents [La Rocca et al., 2008, Patterson et al., 2004]. Clearly, the presence of rings makes determining the properties of the inertial regime in laboratory experiments problematic. Problems arise with analytical and reduced order numerical methods as well. The problem of reconciling the formation of rings and the asymptotic spreading of the gravity current in the inertial-buoyancy equilibrium has been analysed from different perspectives [e.g. Chen, 1980, Garvine, 1984]. A remarkable result was provided by Grundy and Rottman [1986], who demonstrated that no continuous similarity solution satisfying the boundary conditions on the axis of symmetry can exist for the general time-varying inflow axisymmetric problem, except in the case of a constant-volume release.

Consequently, for finite-volume releases, the shallow-water approach provides numerical and analytical solutions to the initial value problem of the axisymmetric spreading of gravity currents, and similarity solutions are identifiable with the asymptotical regimes. Meanwhile, in the case of the continuous release of a fluid spreading axisymmetrically, no continuous analytical solution is available in the context of the shallow-water approximation until the flow enters the late stage of the viscous-buoyancy regime [Huppert, 1982].

A closely related problem, which has successfully been described in terms of viscid shallow-water theory, is the circular hydraulic jump [Bohr et al., 1993]. The problem studied in laboratory experiments and numerical simulations, basically a vertical jet of fluid impinging on a horizontal surface, differs from axial symmetric constant inflow gravity current mainly in that there it is one layer flow, it is stationary with respect to the symmetry axis and the radial current is decelerated mainly due to the effect of viscosity. The theoretical problem has been successfully solved in a classical way imposing a discontinuous solution, or shock, in the sense of Whitham [1999]. A successive experimental investigation by Thorpe and Kavcic [2008] of an internal circular hydraulic jump realised in a two layer flow shows similarities to the conditions studied in axial symmetric constant volume currents, and, in fact, the characteristic outcome of the experiments is the presence of circular, axisymmetric rings. The theoretical line of investigation on circular hydraulic jumps [e.g see Bhattacharjee and Ray, 2011] while providing a general hydraulic model relating the variation of Froude number to the presence of a circular jump in a close analogy with the planar case, does not cover the case of non-stationary, multiple-shocks.

The aim of the present study is to numerically investigate, in the context of the Boussinesq approximation, the formation of three-dimensional lock-exchange flows evolving in axisymmetric, constant-inflow gravity currents and the development of ring structures. Given the initial set-up as described in the experiments of La Rocca et al. [2008], Lombardi et al. [2017], which allows the formation of a constant inflow of dense fluid from the lock, the focus of this study is to investigate the form and evolution of the planform and the propagation of shocks inside the flow in the early stage of development of the gravity current. The presence of an initial slumping phase [Huppert, 1982] and the existence of a subsequent inertial-buoyancy equilibrium regime, consistent with the results of Britter [1979], are then investigated for the purely axisymmetric part of the gravity current.

The thesis is organised in three parts: Part I: Methodology, Part II: Results and Part III: Conclusions. In the first part, after the present general introduction of the state of the art and the overview of some general features of the flow in Chapter 1, the mathematical problem is discussed in Chapter 2. Here the numerical set up is presented and compared with the reference laboratory arrangement. The results of the numerical simulations are presented in Part II. Chapter 3 is focused on the discussion of the axial symmetry of the flow. Chapter 4 concentrates the attention on the formation of hydrodynamical shocks and rings in the flow. Chapter 5 is centred on the analysis of the time evolution of the flow and the determination of the current regimes. A simple extension of the slumping regime theory of Huppert and Simpson [1980] applied to constant-inflow axisymmetric currents is there proposed. The Conclusions are presented in Part III.

Part I

Methodology

Chapter 1

Axial symmetric gravity currents with variable inflow

There are many cases in which axial symmetric gravity currents arise. They can be generated in the field using a fixed volume of fluid in a cylindrical lock (e.g. a release of dense gas in the atmosphere), or using constant volume lock exchange in tanks with divergent lateral walls. In the environment, axisymmetric gravity currents can also be generated by a continuous volume flow source. In this case the propagation of the gravity current has distinctive properties. A few cases are here briefly illustrated in order to highlight the similitudes among them: all of them are caused by a point source providing a continuous inflow with time; they have a definite axial symmetry (if not perturbed by wind or currents); they can be characterised by the presence of rings in the density or temperature field (visible if if analysed with thermal cameras or radiometers).

One of the first studies about axisymmetric gravity currents that are not generated by constant volume sources, is described by Penney and Thornhill [1952]. It investigates the phenomenon called 'base surge', which is found in volcanic eruptions and submarine nuclear explosions. In figure 1.1 the formation of a 'base surge' after the submarine explosion of a nuclear bomb

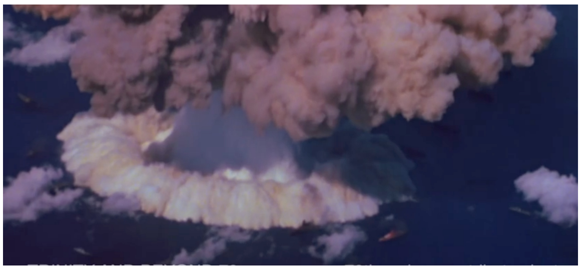

Figure 1.1: Operation Crossroads 'Baker experiment'– base surge formed by nuclear submarine explosion

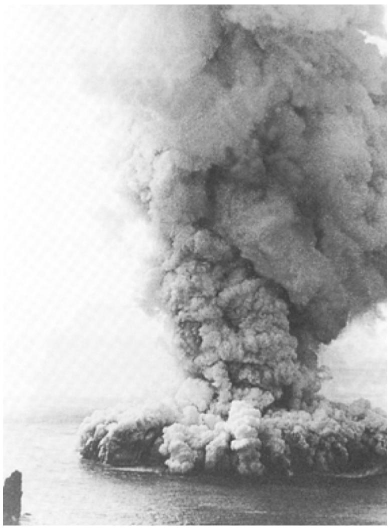

Figure 1.2: base surge generated by volcanic explosion

at Bikini on the 26th of June 1946 is visible as a low circular cloud spreading radially at the base of the high cylindrical column made of water and air which is falling down after the explosion. The tall column of water and air can be considered as a continuous source for the axial symmetric gravity current. The unexpected formation of a fast-spreading base surge caused a large scale radioactive contamination during the experiment. A similar process ('pyroclastic surge') can take place during a volcanic eruption as the one shown in figure 1.2. In the case of pyroclastic surge, the high column, which is the source of the gravity current, is produced by the interaction between magma and water.

Oil slicks are studied since the late sixties in terms of gravity currents propagating at the sea surface. The early results for the spreading of an oil spill generated by a constant volume of oil are summarised in Hoult [1972]. If the spill is generated by a constant inflow of oil, the current is characterised by an amount of pollutant linearly increasing with time. The gravity current generated in this way is considerably faster than the constant volume case, so it spreads over larger distances in the same amount of time. In 2010 an explosion on the Deepwater Horizon offshore drilling station (see figure 1.3) caused the rig to sink on the 22nd of April. The well continued to blowout at the bottom of the sea until 15 July, causing the largest marine oil spill in history (figure 1.4).

Convection episodes, which can produce severe weather, are associated with heating from the ground and instability of the air column. Once the convective cloud develops it can rise to the tropopause, where it is bounded by the temperature inversion. Since there is a continuous flux of moist air rising, the cloud overshoots, expanding radially at the tropopause (in absence

Figure 1.3: Deepwater Horizon rig in flames, 2010

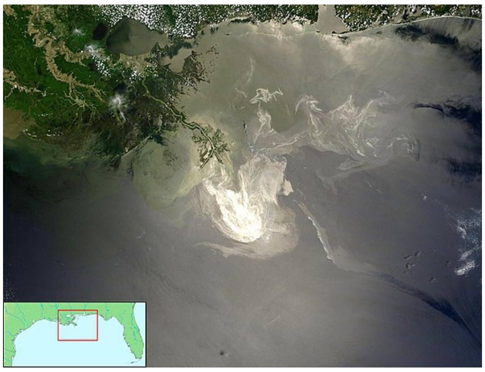

Figure 1.4: Deepwater Horizon oil spill, SAR image over Louisiana 2010

of wind). When the cloud is observed from space (see for example figure 1.5) by a multispectral sensor a combination of information in the infrared band, brightness temperature and in the visible band (‘sandwich’ product) from METEOSAT MSG-2, reveals a central warm core surrounded by a cold ring and again warm ring. This feature is called cold ring cloud (or U cloud in the presence of wind). The correlation between severe weather and the appearance of cold rings is still under investigation. More information may be found in Setvak et al. [2010]

The discharge of freshwater by rivers or estuaries causes surface plumes in coastal waters. In the near field the plumes are shallow, buoyant flows which in some cases spread radially (in the absence of strong wind and currents). In te mentioned conditions, the dynamics is dominated by the gravitational spreading of the thin layer of buoyant water (see for example Garvine [1984]). When the plume is observed in the infrared by a thermal camera it can show consecutive fronts or rings in the temperature field (figure 1.6).

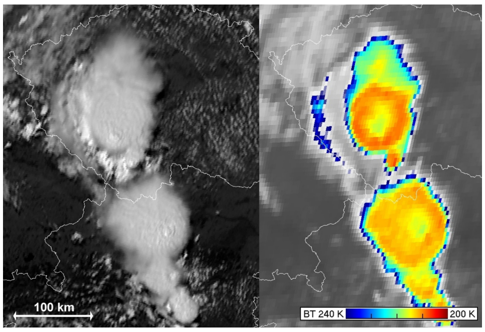

Figure 1.5: 25 June 2006, severe convection over Austria: images from Meteosat MSG2; EUMETSAT training Library

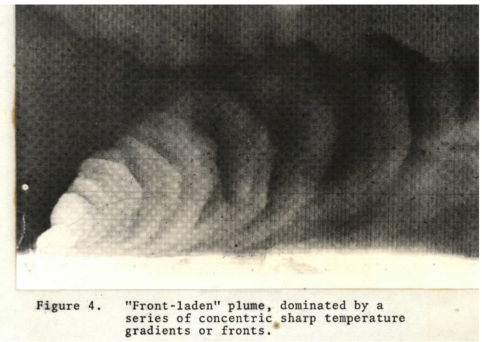

Figure 4. "Front-laden" plume, dominated by a series of concentric sharp temperature gradients or fronts.

Figure 1.6: Thermal scanning of Lake Michigan, 1973, from ‘Application of remote sensing to the investigation of nearshore mixing and coastal entrapment in large water bodies’, Theodore Green IIIa and Robert A. Ragotzkie, in A Progress Report On Multidisciplinary Research On The Application Of Remote Sensing To Water Resources Problems, 1972-1973, NATIONAL AERONAUTICS AND SPACE ADMINISTRATION, Office of University Affairs Washington, D.C. 20546

Chapter 2

Problem description

2.1 Numerical formulation

A large eddy simulation model is used to solve the filtered Navier-Stokes equations under the usual Boussinesq approximation. Considering a Cartesian coordinate system with spatial components x_i and time t, the flow variables are denoted as u_i for the velocity field and ρ for the density field. The reference frame has the x_3 coordinate parallel and opposite to the the gravity force and the other two coordinates (x_1, x_2) accordingly defined on the plane orthogonal to x_3. Following Salmon [1998], $\rho_{tot}(x_i, t)$ is subdivided into a constant term $\langle\rho\rangle$, a static term $\tilde{\rho}$ that depends only on the vertical component $(x_i\delta_{i3})$, and a residual density $\rho'(x_i, t)$:

$$\rho_{tot}(x_i, t) = \langle\rho\rangle + \tilde{\rho}(x_i\delta_{i3}) + \rho'(x_i, t) \qquad i = 1, 2, 3. \tag{2.1}$$

The pressure field can be decomposed as

$$p_{tot}(x_i, t) = \tilde{p}(x_i\delta_{i3}) + p'(x_i, t) \tag{2.2}$$

since it appears in the equations under the sign of a gradient. In the expressions above, the Kronecker tensor δ_{ij} has been used, where

$$\left.\begin{array}{lll} \delta_{ij} = 1 & \text{if} & i = j \\ \delta_{ij} = 0 & \text{otherwise} & \end{array}\right\} \tag{2.3}$$

In the Boussinesq approximation it is assumed that :

$$\langle\rho\rangle \gg \tilde{\rho}(x_i\delta_{i3}) \gg \rho'(x_i, t), \qquad \tilde{p}(x_i\delta_{i3}) \gg p'(x_i, t). \tag{2.4}$$

Considering a system in which the field of density ρ varies in the closed range $[\rho_2, \rho_1]$, where the difference $(\rho_1 - \rho_2) > 0$ is small, and defining $\Delta\rho = \rho_1 - \rho_2$, $\epsilon = \frac{\Delta\rho}{\rho_2}$, and $g' = \epsilon g$, the Boussinesq approximation is applied assuming that $\Delta\rho \sim \rho'$ and $\rho_2 = \langle\rho\rangle$. As usual, g is gravitational acceleration, and g' is

reduced gravity.
To consider a suitable non-dimensional form of the equations, it is assumed that the dimensional variables x_i, t, u_i, p are related to the dimensionless corresponding variables x_{i*}, t_*, u_{i*}, p_* through the scales L_s, T_s, U_s in the following way: $x_i = L_s x_{i*}$, $u_i = U_s u_{i*}$, $t = T_s t_* = L_s/U_s t_*$ and, if H is the total height of the physical volume, $p' = \Delta\rho g H p'_* = \rho_2 \epsilon g H p'_* = \rho_2 g' H p'_*$. In addition, $\frac{\rho'}{\rho_2} = \frac{\Delta\rho}{\rho_2}\rho'_*$, i.e. $\frac{\rho'}{\rho_2} = \epsilon\rho'_*$. The choice of the consistent set of scales $L_s = H$, $U_s = \sqrt{g'H}$ and $T_s = \frac{H}{U_s}$ produces the momentum equation in non-dimensional form, where all asterisks and primes are dropped to make the notation lighter, and the compatibility with the hydrostatic equation for i=3 eliminates $\tilde{p}$ and $\tilde{\rho}$:

$$\frac{\partial u_i}{\partial t} + \frac{\partial u_j u_i}{\partial x_j} = -\frac{\partial p}{\partial x_i} + \frac{1}{\sqrt{Gr}}\frac{\partial^2 u_i}{\partial {x_j}^2} - \rho\delta_{i3}. \tag{2.5}$$

The scale velocity U_s is of the order of magnitude of the buoyancy velocity, but given that the gravity current has a depth $h(x_i, t)$which is almost always much less deep than H/2, the value of the actual buoyancy velocity is a function of time and position in the flow. The Grashof number $Gr = \left(\frac{U_s H}{\nu}\right)^2$ is clearly related to the Reynolds number when the latter originates from a different choice of the set of scales, i.e. $U_s = U_f$, where U_f is the front velocity and L_s is expressed in terms of a measure of the height of the current at the front h_f, i.e. $L_s = h_f = \alpha H$ [Härtel et al., 2000]. Then,

$$Re = \frac{U_f h_f}{\nu} = \frac{\alpha U_f}{U_s}\frac{U_s H}{\nu} = \alpha Fr_f \sqrt{Gr} \tag{2.6}$$

where Fr_f is a Froude number that depends on the velocity of the front-line of the gravity current and $0.0 < \alpha < 1.0$ a numerical coefficient.

After applying the LES filtering procedure, the complete system takes the following form:

$$\frac{\partial \bar{u}_j}{\partial x_j} = 0 \tag{2.7}$$

$$\frac{\partial \bar{u}_i}{\partial t} + \frac{\partial(\bar{u}_j\bar{u}_i)}{\partial x_j} = -\frac{\partial \bar{p}}{\partial x_i} + \frac{1}{\sqrt{Gr}}\frac{\partial^2 \bar{u}_i}{\partial x_j \partial x_j} - \bar{\rho}\delta_{i3} - \frac{\partial \tau_{ij}}{\partial x_j} \tag{2.8}$$

$$\frac{\partial \bar{\rho}}{\partial t} + \frac{\partial(\bar{u}_j\bar{\rho})}{\partial x_j} = \frac{1}{\sqrt{Gr}Sc}\frac{\partial^2 \bar{\rho}}{\partial x_j \partial x_j} - \frac{\partial \lambda_j}{\partial x_j} \tag{2.9}$$

where Sc is the Schmidt number, defined as $Sc = \nu/k$. ν is the kinematic viscosity and k is the diffusivity for a saline solution at environmental temperature and salinity associated with the required density. Given a generic field $\phi(x_i, t)$, the symbol $\bar{\phi}$ denotes the filtering operation, which is

performed here through implicit application of the top-hat filter. All the mentioned variables with overhead are resolved-scale filtered quantities. In particular, $\bar{\rho}$ is now intended to be the filtered dimensionless residual density caused by the salinity variation in the absence of ambient stratification and at constant temperature. In fact, the density here is directly related to the concentration of salt by a linearised state equation in terms of a volumetric coefficient β.
The sub-grid-scale momentum flux contribution, defined as

$$\tau_{ij} = \overline{u_i u_j} - \bar{u}_i \bar{u}_j \tag{2.10}$$

and the sub-grid-scale mass flux

$$\lambda_j = \overline{\rho u_j} - \bar{\rho}\bar{u}_j \tag{2.11}$$

are computed using the dynamic Lagrangian model of Meneveau et al. [1996]. The choice of the Lagrangian model is motivated by the absence of directions of homogeneity in the development of three-dimensional gravity currents. In the model, equations (2.7)-(2.9) are written in curvilinear coordinates and numerically integrated using the fractional step algorithm of Zang et al. [1994]. In applications on orthonormal grids the algorithms are simplified and the equations are solved on a completely Cartesian geometry. A more general and exhaustive description of the numerical methods used can be found in Armenio and Piomelli [2000] and Armenio and Sarkar [2002]. The model has been successfully applied in boundary layer studies [Salon et al., 2007, Taylor et al., 2005] and, more recently, in the evaluation of mixing in planar gravity currents [Ottolenghi et al., 2016a,b, 2017]. The present version of the model utilises an immersed boundary technique [Roman et al., 2009] to simulate the presence of obstacles in the domain of the flow. No-slip boundary conditions are imposed for velocity on the bottom and on the lateral walls, whereas on the top wall, a shear-free boundary condition is applied. No-flux conditions are also enforced for the salinity on all boundaries.

2.2 Numerical implementation

The simulations aim to realistically reproduce experimental conditions similar to those described in La Rocca et al. [2008, 2012], Lombardi et al. [2017]. For simplicity, the indicial notation is dropped in the following in favour of the basic Cartesian notation: $x = x_1$, $y = x_2$, and $z = x_3$. Consistently, for the flow velocity components, u_1 will be denoted as u, $u_2 = v$, and $u_3 = w$. The geometry of the experimental apparatus has been numerically reproduced in the form of a rectangular tank of length L, width $2y_0$ and height H, with the vertical dimension H being considerably smaller than the horizontal ones (y_0 and L). The domain of the simulation is the entire

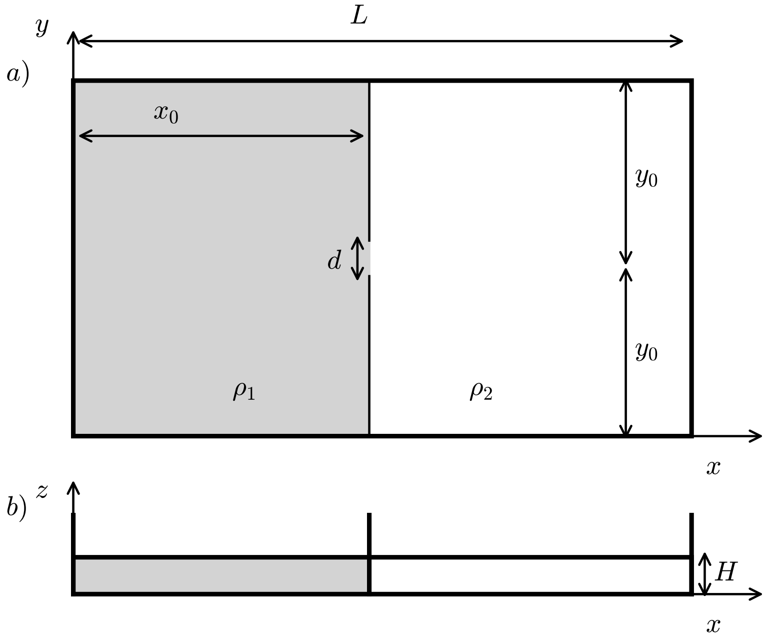

Figure 2.1: Sketch of the lock-release tank: (a) top view and (b) side view.

volume of a tank $L \cdot 2y_0 \cdot H$. The tank is divided into two volumes by a wall inserted at a distance of x_0 from the left side of the tank. An open gate of length d is positioned at the centre of the separating lock wall. The ratio between the width of the gate and the size of the wall is $d/y_0 \ll 1$. The initial conditions are the fluid is at rest everywhere, and the left-hand side of the tank is filled with a relatively dense solution of salt in water at ρ_1, while on the opposite side of the tank, there is freshwater at ρ_2. A schematic of the geometry of the numerical domain and the laboratory tank for the LD case is shown in figure 2.1. Two different configurations are implemented: one closely corresponds to the laboratory experiments mentioned above, and the other, which would be hardly realisable in ordinary laboratory conditions, simulates an extended domain to follow the numerical spreading for relatively long times. The values of the geometrical parameters for the two domains, i.e. the laboratory domain (LD) and the extended domain (ED), are shown in table 2.1. The primary difference between the two domains is that in the ED the circular frontline is able to develop over a horizontal area approximately 9 times larger than in the LD case.

The simulation begins with the left volume (i.e. the lock) filled with a liquid with density ρ_1 (a solution of sodium chloride, NaCl, and fresh water in the physical experiments) and the right volume filled with a liquid with a lower density ρ_2 (fresh water in the physical experiments). Both portions of the tank are filled to the same level $h_0 = H$ (full-depth configuration). The

Geometry	L	$2y_0$	H	x_0	d	$\frac{d}{2y_0}$
LD	16.8	9.6	1.0	8.0	0.96	0.10
ED	35.7	21.4	1.0	14.3	0.96	0.05

Table 2.1: Geometrical parameters for the laboratory domain (LD) and the extended domain (ED).

presence of the separating wall with the lock opening d has been implemented in the simulation by imposing no-slip condition on the nodes contained in the wall, except for the grid points on d. The condition has been realised by using an immersed boundary technique as described in Roman et al. [2009]. The three-dimensional grid for the LD domain is composed of $1024 \times 64 \times 512$ cells in the x, y, z directions, respectively and it is not uniform. On the horizontal plane (x, y), the grid has the highest resolution $\Delta x = 0.01$; $\Delta y = 0.01$ in the central part of the domain, near the separating wall; and it has a lower resolution towards the external vertical walls. Along the vertical dimension, z, it has maximum resolution at the top and bottom of the domain, with a relatively coarse resolution in the central part. The cells in the three directions are distributed as $arctan(x_i)$ following the method of Vinokur [1983]. The rationale for this choice is that, since the current is generated by lock exchange, there are two almost symmetrical currents propagating in opposite directions, one is a current made of dense fluid propagating on the bottom of the tank in the positive x-direction, the other is a current of light fluid propagating on the top of the tank in the negative x-direction. Both are important in determining the volume discharge at the gate. As shown in figure 3.1, both the currents on the top and on the bottom of the tank move respectively below and over the plane at $z = 1/2$ during the whole simulation.

The numerical grid on the ED domain, made of $2048 \times 64 \times 1024$ nodes, is an expanded version of the previously described one. It has the same structure in the vertical z direction and a non-uniform horizontal grid with the same higher resolution Δx, Δy near the gate and the same lower resolution near the external wall. The LES on the extended grid requires very high-performance computing resources, and the results were obtained on a cluster of high-performance computing nodes using 512 cores.

In all simulations, it was verified that the grid resolution is sufficiently fine to resolve the near-wall structures, as required by wall-resolved LES. In particular, it was verified that the dimensionless grid size in terms of wall units $x_i^+ = \frac{x_i u_\tau}{\nu}$ is always in the range $\Delta x^+ < 20$, $\Delta y^+ < 50$, and $\Delta z^+_{max} \simeq 1$, where u_τ is the local friction velocity [Piomelli and Balaras, 2002, Piomelli and Chasnov, 1996]. A post-processing of the velocity field and the field of τ from the sub-grid turbulence model was used in order to verify that the conditions were met for all grids and all flows. The condition that a sufficient number of points fell in the inner region of the vertical profile of velocity was verified as well.

2.3 Test cases

Eleven test cases were simulated, the field of variation of the parameters is shown in table 2.2. Cases S1–S6 have Gr increased by three orders of magnitude from $Gr(\mathrm{S1}) = 8.1 \cdot 10^4$ to $Gr(\mathrm{S6}) = 2.0 \cdot 10^8$, i.e. raised by a factor of 2500. Cases S7–S11 have Gr in the range $[2.7 - 8.1] \cdot 10^8$, i.e. Gr is increased by a factor of 3 from S7 to S11. Case S12 is a laboratory experiment conducted under the same conditions as case S11.

The full-depth release of saline gravity currents was conducted at the Hydraulics Laboratory of the University of 'Roma Tre' in a rectangular Plexiglas tank with the same dimensions and configuration shown in figure 2.1. The physical length of the tank is 2.35 m, width 1.35 m and height 0.14 m. A blue dye (methylene) was added to the salty solution (i.e. the lock fluid) to identify the two fluids during the experiment. The density measurements were performed using a pycnometer, with a relative error 0.2%. The experiment started when the lock-gate was lifted vertically. The development of the current was recorded using an overhead charged coupled camera, with a time resolution of 25 fps and a spatial resolution of 0.25 cm/pxl. The space-time evolution of the current shape was measured by applying an image analysis technique based on the threshold method [Adduce et al., 2012, Lombardi et al., 2015]. Points belonging to the current profile (i.e. interface between the two fluids) were determined within an error of 0.2 cm. An additional simulation, S13, was conducted to consider the spreading on the ED larger scale. The same fluid properties as in case S9 were used in the larger domain ED.

A key parameter of the gravity current dynamics is the flow rate of dense fluid at the separating gate, Q. This flow rate directly affects the speed of the front of the current and the onset of the viscous regime, which was estimated as $t_v \sim \sqrt{\frac{Q}{g'\nu}}$ by Huppert [1982] in the limit of the shallow water approximation and experimentally by Britter [1979]. To compute Q, the average longitudinal component of the flow velocity, $u_0(t)$, is evaluated as the average of the positive longitudinal velocity in the plane (y, z) at x_0 (the open section of the dividing wall). The longitudinal flow rate $Q(t)$ at x_0 is then evaluated as $u_0(t) \cdot \Sigma_{u>0}(t)$, where $\Sigma_{u>0}(t)$ is the surface crossed by the positive u component in each numerical simulation.

In all simulations, the flow rate exhibits a peak in the very early stage of development and then tends to an almost constant value after a relatively small time which varies from one case to another. The non dimensional volume discharge $\frac{Q}{U_s H^2}$ is independent of Gr at relatively high Grashof numbers,

	Gr	ϵ	$\frac{Q}{U_s H^2}$	η	t_0	t_i	t_v	t_f
S1	$8.1 \cdot 10^4$	0.030	(0.156 ± 0.001)	-	4.8	4.8	6.7	47.8
S2	$5.0 \cdot 10^5$	0.030	(0.169 ± 0.001)	-	3.5	5.2	10.9	31.9
S3	$2.0 \cdot 10^6$	0.030	(0.175 ± 0.001)	-	2.9	5.4	15.8	30.7
S4	$4.5 \cdot 10^6$	0.030	(0.1780 ± 0.001)	-	4.1	5.4	19.4	27.5
S5	$8.1 \cdot 10^6$	0.030	(0.1792 ± 0.001)	-	3.2	5.5	22.5	26.1
S6	$2.0 \cdot 10^8$	0.030	(0.180 ± 0.003)	0.55	2.9	5.5	50.3	26.1
S7	$2.7 \cdot 10^8$	0.010	(0.180 ± 0.001)	0.48	3.3	5.4	54.2	21.6
S8	$4.0 \cdot 10^8$	0.015	(0.180 ± 0.001)	0.49	3.1	5.5	60.4	22.6
S9	$5.4 \cdot 10^8$	0.020	(0.180 ± 0.002)	0.51	3.1	5.6	64.6	21.3
S10	$6.7 \cdot 10^8$	0.025	(0.180 ± 0.003)	0.45	2.9	5.6	68.2	19.9
S11	$8.1 \cdot 10^8$	0.030	(0.179 ± 0.003)	0.48	2.9	5.5	71.8	21.5
S12	-	0.030	-	-	-	5.5	71.8	19.2
S13	$5.4 \cdot 10^8$	0.020	(0.187 ± 0.003)	0.51	3.1	5.6	64.6	68.7

Table 2.2: S1–S11: numerical simulations in the LD, S12: laboratory experiment in the LD, and S13: numerical simulation in the ED

i.e. for $Gr > 10^6$ (see table 2.2 and figure 3.2). The dimensionless volume discharge and the transient time t_0 are related, as the non dimensional volume $\frac{Qt_0}{H^3}$ does not show any dependence on the Grashof number.

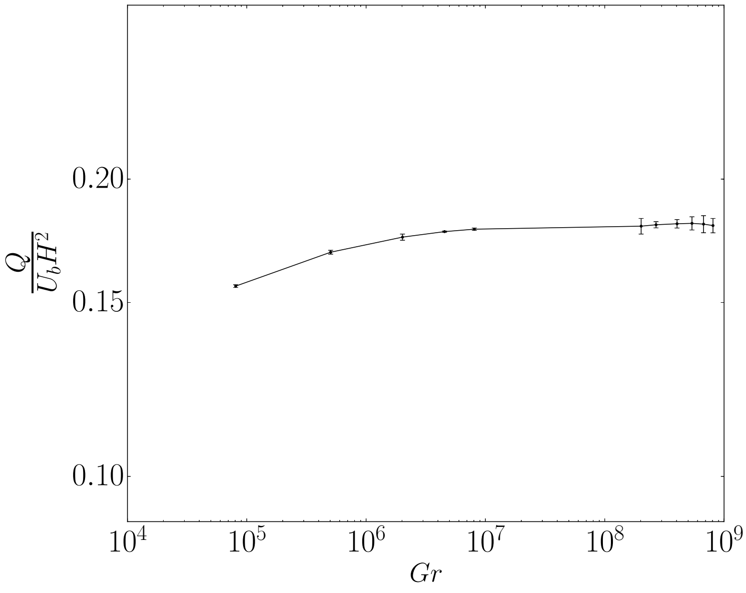

Figure 2.2: Nondimensional volume flow vs. Gr

Part II

Results

Chapter 3

Axial symmetry

Immediately after the transient time, a heavy current develops on the bottom surface in the right part of the tank, where the ambient fluid is fresh water. A similar and almost symmetrical buoyant current is generated on the top surface on the opposite side of the tank, as shown in figure 3.1. The two currents present similarities and differences: both manifest axial symmetry and instabilities, but the current spreading on the bottom is more stable and is simpler to investigate in laboratory (see subsection 4.3). Consequently, only the spreading of the current on the bottom of the tank is considered in the following, unless explicitly stated. In order to discuss the axial symmetry of the frontline it is necessary to formalise the definition of some geometric constructions which are used in both the numerical and experimental analisys. The external contour of the planform, taken as the frontline of the current, can be determined using the field of density on a fixed horizontal plane by introducing a threshold value ψ. Then a plane function G is readily obtained which has the definition

$$\left.\begin{array}{llll} G(x,y)=1 & \text{on} & (x,y) \quad | & \dfrac{\rho(x,y,z_b)-\rho_2}{\rho_1-\rho_2}-\psi <= 0, \\ G(x,y)=0 & \text{otherwise} & & \end{array}\right\} \tag{3.1}$$

The external frontline is identified implicitly by the function $G(x, y)$ defined on the horizontal plane $z = z_b = 0.05$. This is the lower height at which the velocity profile is not significantly affected by the distance from the bottom, particularly by the radial structures associated with the time evolution of lobes and clefts. The determination of the minimum plane height is important as the depth of the current becomes very shallow during the spreading. ψ is a small density threshold used in the determination of the frontline. The frontline position can be determined in low Gr cases starting from $\psi = 1\%$, but taking $\psi = 3\%$ provides a sufficiently continuous frontline in all cases.

In the experiment S12, the frontline is determined using a threshold method, fully described in [Lombardi et al., 2017], applied to the images

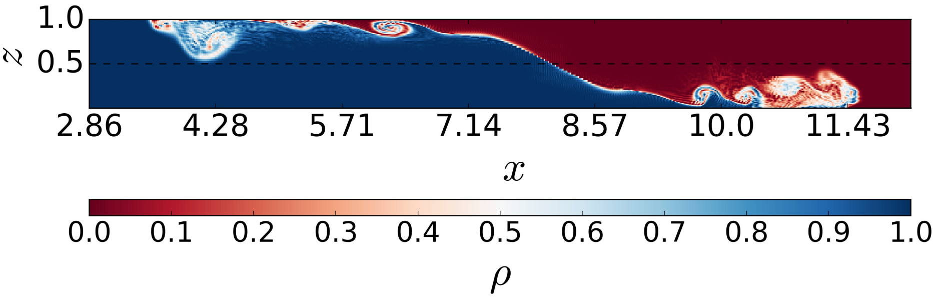

Figure 3.1: Density field on the midplane $y = y_0$, $t = 8.7$, case S11

recorded by an overhead camera. The implicit function $G(x, y)$ can be used to obtain the explicit form of the frontline $x_f = f_l(y)$ on the fixed horizontal plane, starting by identifying separately the maximum and minimum of the frontline function above and below the longitudinal axis. At all times, the form of the frontline has a definite curvature: at the starting time it is close to elliptic, with the radius in the transverse (y) direction being greater than that in the longitudinal (x) one. The elliptic form of the frontline collapses to a circle in a short time, and the frontline maintains the circular shape in time despite occasional perturbations.

The simplest approach to identify the frontline explicitly is then to consider the two radii of curvature, R_b along y and R_a along x. In general, if the frontline is an ellipse (or a circle), then the maximum and minimum of G will have the same projection on the x axis, i.e. x_c. The minor semi-axis of the ellipse, b, is taken as half the distance between the two points. The major axis of the ellipse, a, is then obtained from the difference between the intersection of the frontline with the x axis, x_f, and the x-coordinate of the centre, x_c. The geometry of the spreading is illustrated in figure 3.2 showing the frontline G at the end of the simulation in the low Grashof number case S2. An accurate examination immediately reveals that the frontline has a circular shape centred at a position x_c on the longitudinal axis $y = y_0$. In other words, as shown below, the current assumes an axial-symmetric form with respect to a time-varying virtual origin that translates along $y = y_0$. The major difference among the low Gr cases S1–S4 is the rate of increase of $x_c(t)$. In case S1, the position $x_c(t)$ increases almost linearly in the first $\Delta t = 10$ up to $x_c = 1.1$, and then it remains almost constant. In case S2, as shown in figure 3.3, $x_c(t)$ increases monotonically in the first $\Delta t = 14$, up to $x_c = 1.4$. In case S3, $x_c(t)$ increases monotonically during almost all the simulation ($\Delta t = 26$) up to $x_c = 2.1$. In case S4, $x_c(t)$ increases monotonically in the first $\Delta t = 14$ of the simulation up to $x_c = 1.8$. Between $t = 10$

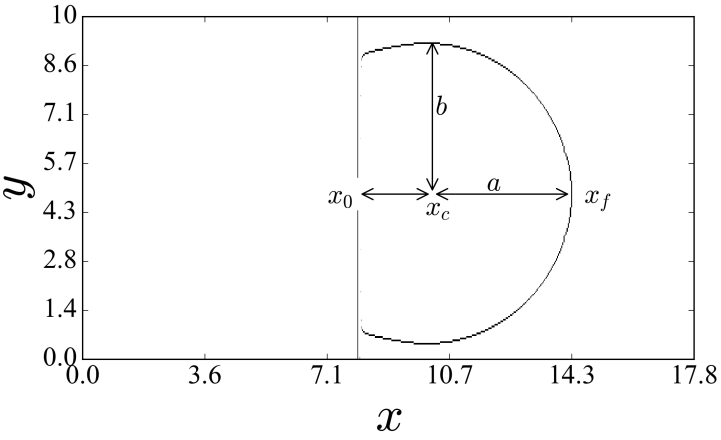

Figure 3.2: Case S2 $Gr = 5.0 \cdot 10^5$, $\epsilon = 0.03$; frontline $G(x, y)$ at t=32

and 13, very small jumps in x_c in cases S3 and S4 can be associated with the development of minor lobe and cleft instabilities along the frontline (not shown).

In fact, in some cases, the maximum and minimum of the frontline function $x = f_l(y)$ may correspond to the position of the larger lobe formed near the top and/or the larger lobe near the bottom. In time, the position of the maximum/minimum would then follow the position of the lobe rather than the radius of curvature and lag progressively behind until the lobe vanishes. After the lobe disappears, the new position of the maximum is found relatively far from the previous one. Consequently, the behaviour of $x_c(t)$ appears to be discontinuous or exceedingly irregular.

For $4.5 \cdot 10^6 < Gr < 10^7$, the lobes are relatively few and larger, whereas for $Gr > 10^7$, the number of lobes increases, but the frontline is less perturbed. Since the life span of the individual lobes is on the order of $\Delta t \sim 3$, i.e. small compared to the duration of any simulation or experiment, a correction for the estimate of the radius of the circular frontline and the position x_c of the centre along the x axis can be implemented. An effective method is proposed in Appendix A. The correction can be applied to all cases in which lobes and clefts significantly perturb the frontline, particularly in the first part of the current development, i.e. mostly cases S5–S12.

The results of the extended domain simulation S13, as shown in figure 3.4, indicate that in the long period, the radius R increases regularly and monotonically with time, whereas the centre of the frontline (x_c,y_0) moves more slowly, having speed small and almost constant at relatively large times, i.e. for $t > 20$. The latter is displaced along the x axis by $\delta x_c = 2$ in

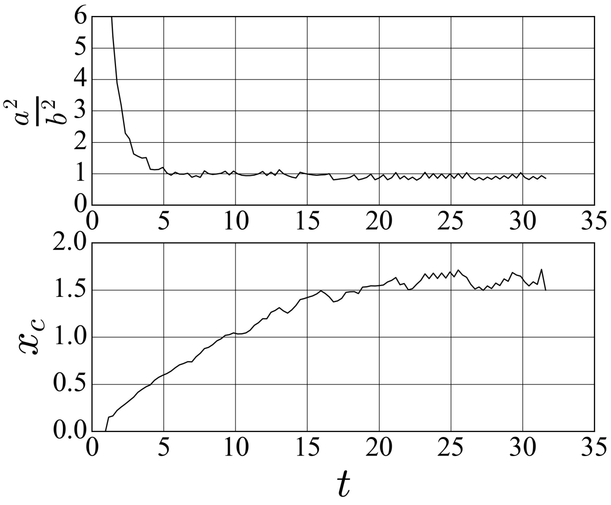

Figure 3.3: Case S2: $Gr = 5.0 \cdot 10^4$, $\epsilon = 0.03$; top panel: $\frac{a^2}{b^2}$ vs. t; bottom panel: $x_c(t)$ vs. t

the first $\Delta t = 20$ (as in S9) and then only by $\delta x_c = 1.5$ in the next $\Delta t = 40$.

The correction procedure is also applied to the frontline obtained from the images of the experiment in the (x, y) plane, viewed from a camera positioned above the tank. The evolution in time of the frontline and the corrected radius are shown in figure 3.5. Although the frontline is defined differently, i.e. the planform of the experiment is a top view of the dyed fluid, whereas the planform of the simulations is a cross section of the density field, the results are very similar to those obtained for numerical simulation S11. The three-dimensional lock exchange experiments described in Lombardi et al. [2017], which were realised in the conditions described by the LD domain (as in figure 2.1), were focused on the variation of the lock gate and depth of the fluid. Differences with respect to the here considered set up are in the total depth of their initial current, $H = 1.1$ and $H = 0.7$, and in the value of the gate width, resulting in the ratios $\frac{d}{2y_0} = 0.1$, $\frac{d}{2y_0} = 0.26$ and $\frac{d}{2y_0} = 0.5$. In the case of $\frac{d}{2y_0} = 0.1$, $H = 1.1$, the results they show are very similar to the results found in our cases S7, S11 and S12 in terms of shape and evolution of the frontline. The current becomes axial-symmetric after a short time and the front propagation with time is always decelerating in a nonlinear way. They found instead that, at high $Gr \sim 8.0 \cdot 10^8$, for $\frac{d}{2y_0}$ >= 0.5, the frontline maintains flat in the direction parallel to the gate for all the time it take for the frontline to reach the lateral boundary. The frontline propagates in the mid plane along the x axis at a constant speed, as is characteristic in the planar slumping. At smaller total depth, $H = 0.7$ and smaller Grashof number, $Gr \sim 3.0 \cdot 10^8$, the axial symmetry

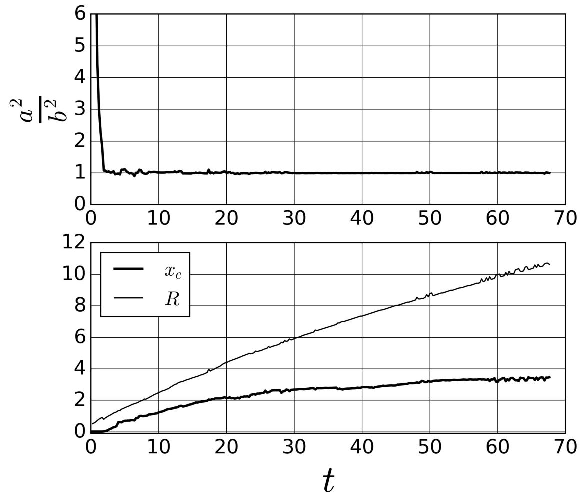

Figure 3.4: Case S13: $Gr = 5.3 \cdot 10^8$, $\epsilon = 0.02$; top panel: $\frac{a^2}{b^2}$ vs. t; bottom panel: $x_c(t)$ and $R(t)$ vs. time

is lost at a smaller gate width, $\frac{d}{2y_0} >= 0.25$. The dimension of the tank does not allow to guess if and to which extent an eventual axial symmetry of the frontline is reached at longer times. Notably, the results here discussed are similar to those of Maxworthy [1980], who performed experiments with three-dimensional lock-exchange collapsing fluids in a stratified ambient fluid. In the mentioned study, the flow could be separated in a radial expansion and a rigid translation not only for the current's front but also for the ring-like solitary waves propagating ahead on the interface between two fluid layers (see figure 16 in the original paper).

In the following sections, the symbol R represents the radius of the axial symmetric current obtained from three-dimensional lock-exchange currents as previously described, whereas r indicates the radius of an equivalent axial symmetric current generated by a constant inflow at the axial position [as in Britter, 1979]. In order to study the properties of the purely axial symmetric part of the current, the velocity field u is decomposed in a plane translating velocity field $\dot{x}(t)_f$ and an axial symmetric velocity field u_r, u_θ, u_z obtained, by applying the ordinary transformation rules for first-order tensors from a Cartesian (x, y, z) to a cylindric coordinate system (R, θ, z). θ is, of course, the azimuthal angle.

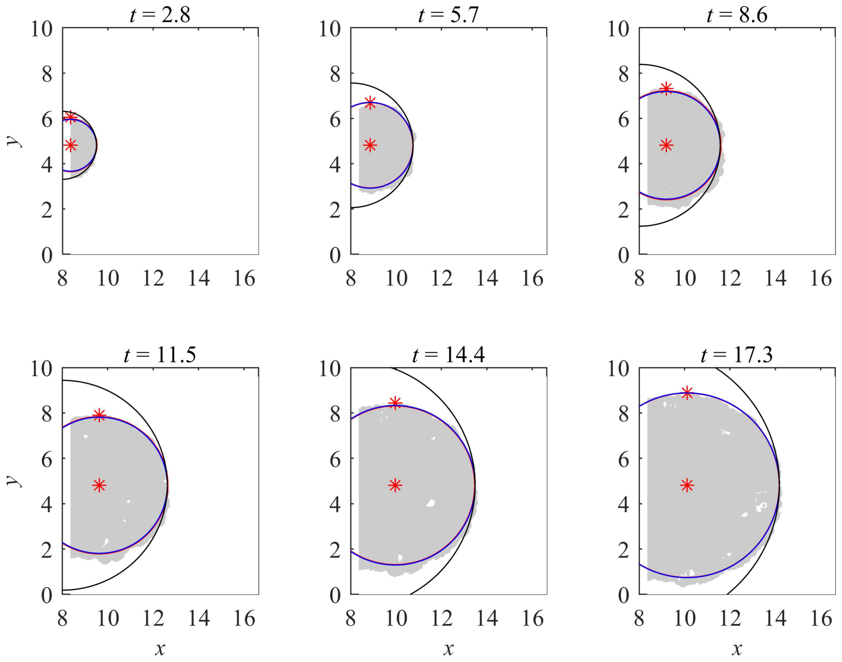

Figure 3.5: Case S12 (experiment) evolution in time of the frontline at $t = 2.8$, 5.7, 8.6, 11.5, 14.4, and 17.3; grey area is the planform of the gravity current; black line: circle centred at the centre of the separating gate and radius equal to the distance from the gate to the frontline on the x axis; blue lines: circles centred at x_c and radius $R_b = R_a$; asterisks: position of the centre (x_c, y_0) and of the upper extremal (x_c, y_+)

Chapter 4

Rings

4.1 Low Grashof number

In case S1, $Gr = 8.1 \cdot 10^4$, the current at the bottom assumes an almost circular frontline and spreads uniformly. In a later stage of development, the presence at the bottom of coherent radial structures where the vertical velocity is positive suggests the formation of early lobe and cleft instabilities. Here, the ambient fluid trapped under the bottom layer of the advancing current finds its way upwards. The structures are limited in extent to the immediate proximity of the bottom, and the form of the frontline does not significantly deviate from a circle. The development of periodic structures in the flow may be followed using Hovmoller diagrams (HDs) in the density ρ field. In the analysis of the numerical simulations, HDs are created using the time-varying density field $\rho(x, y_0, z_c, t)$ on the centreline of the tank at the point $z_c = 0.12$, $y = y_0$. The diagram is relatively sensitive to the choice of the vertical level z_c in the sense that, mostly due to the continuously decreasing depth of the current, selecting level too low would provide discontinuous bands, particularly in the area close to the axis, and a level too high would make appear the bands to merge early. In the HDs, the density field extracted at the centreline is mapped in the space (x, t). Periodic perturbations in the density field appear in a diagram with a series of alternating bands having different colours. As shown in figure 4.1, at very low Gr there is no indication of perturbations in the density field, except for the advancement in time of the external frontline. An increase in Grashof number enhances the formation of lobe and cleft instabilities, which in case S2 appears to significantly alter the symmetry of the external front. The lobes and clefts at the front are now clearly connected with the radial structures, forming complex three-dimensional networks close to the bottom.

In S3, at approximately $t \sim 7$ from the start of the simulation, the flow near the front appears to develop a configuration of the radial velocity field

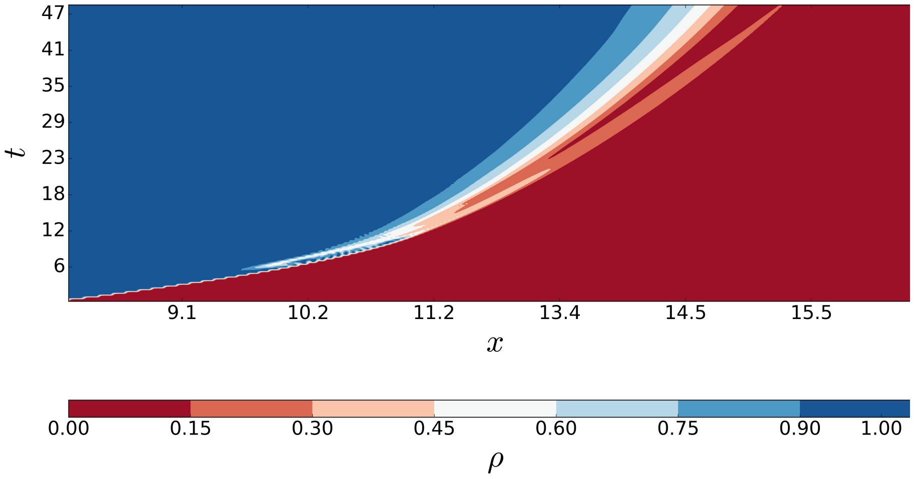

Figure 4.1: Hovmoller diagram, case S1, simulation $Gr = 8.1 \cdot 10^4$

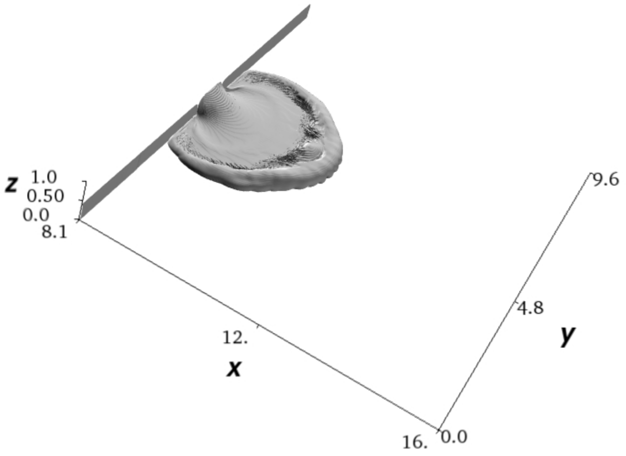

z
1.0
0.50
0.0
8.1
12.
x
16.
0.0
4.8
y
9.6

Figure 4.2: Density isosurface at $\rho = 3\%$, case S3, $t = 8.7$

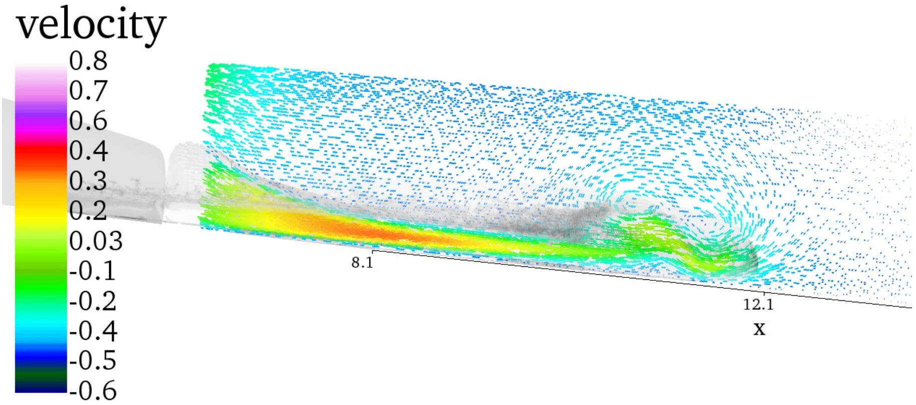

Figure 4.3: Density isosurface at $\rho = 3\%$ and velocity field on the mid plane (x, z), case S3, $t = 8.7$

similar to a breaking wave. The analysis of the u_r field reveals an ascending band followed by an abruptly descending one. This result is due to the interaction between the external front and a successively generated internal shock that follow closely. The external front structure assumes toroidal features in the horizontal plane, stretching out from the body of the current (figure 4.2). The local maximum of velocity appears at the ascending part of the tube and is coupled with a Kelvin-Helmholtz billow structure external to the dense current in the ambient fluid. A second billow very close to the first one is visible near the external front (figure 4.3).

A Froude number $Fr_H = \frac{\bar{u}_r}{\sqrt{\overline{g'h}}}$ [Shin et al., 2004] is introduced in terms of vertically averaged, radial component of velocity $\bar{u}_r$ and the local average buoyancy velocity $U_l = \sqrt{\overline{g'h}}$, where $\overline{g'h} = g \int \frac{\rho(x,y,z)-\rho_2}{\rho_1} dz$. Defined in this way, Fr_H is the ratio between the vertically averaged radial outward velocity and the group velocity of the most rapid waves propagating inward at the interface, measured relative to the mean outward flow. When $Fr_H > 1$ no information can propagate backward toward the symmetry axis, and, as in the planar case, a sudden circular jump in the depth of the fluid is expected between the annular region at high velocity and another region with lower velocity [Bhattacharjee and Ray, 2011, Thorpe and Kavcic, 2008]. The kinematics of the flow on the mid plane $y = y_0$ is highlighted in figure 4.4 by the modulus of the fluid velocity vector scaled by U_l, i.e. $\frac{|\vec{u}|}{\sqrt{\overline{g'h}}}$. The introduction of the local buoyancy scale provides a method for evaluating the depth of the current that does not depend on a fixed threshold in the density field, $h_l = \frac{\overline{g'h}}{g'}$. A second height h_t is calculated as the height of the

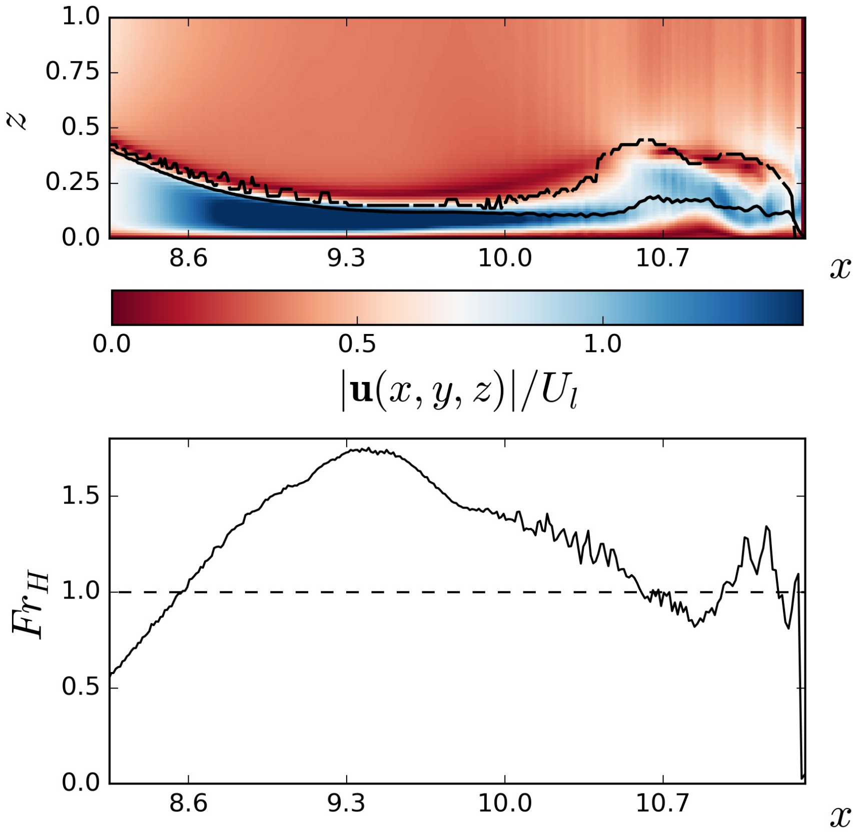

Figure 4.4: top: non dimensional radial velocity $\frac{|\bar{u}|}{U_l}$ on the mid-plane $y = y_0$; the continuous black line indicates the depth $h_l = \frac{\overline{g'h}}{g'}$ and the broken black line marks h_t, i.e. the interface $\rho = 3\%$, bottom: Froude number Fr_H vs. x. Case S3, $t = 8.7$

$\rho = 3$ % isopycnal. While h_l remains well under the depth at which mixing is effective, as discussed by Shin et al. [2004], h_t is largely affected by mixing with the ambient fluid, so where the two curves diverge in figure 4.4, then entrainment must have occurred. In the initial development of the current, the flow has a $Fr_H > 1$ in a disk around the axis, it shows a transition to $Fr_H < 1$ around x=10.5 and shows again $Fr_H > 1$ in a small ring at the head of the current. This behaviour is consistent with the presence of the circular hydraulic jumps in the core of the current shown by the line h_l. The depth indicated by the line h_t is instead mostly related to the action of the Kelvin-Helmoltz billows.

At successive times, the value of u_r behind the front decreases in intensity with R, and its distribution becomes more uniform along the body of the

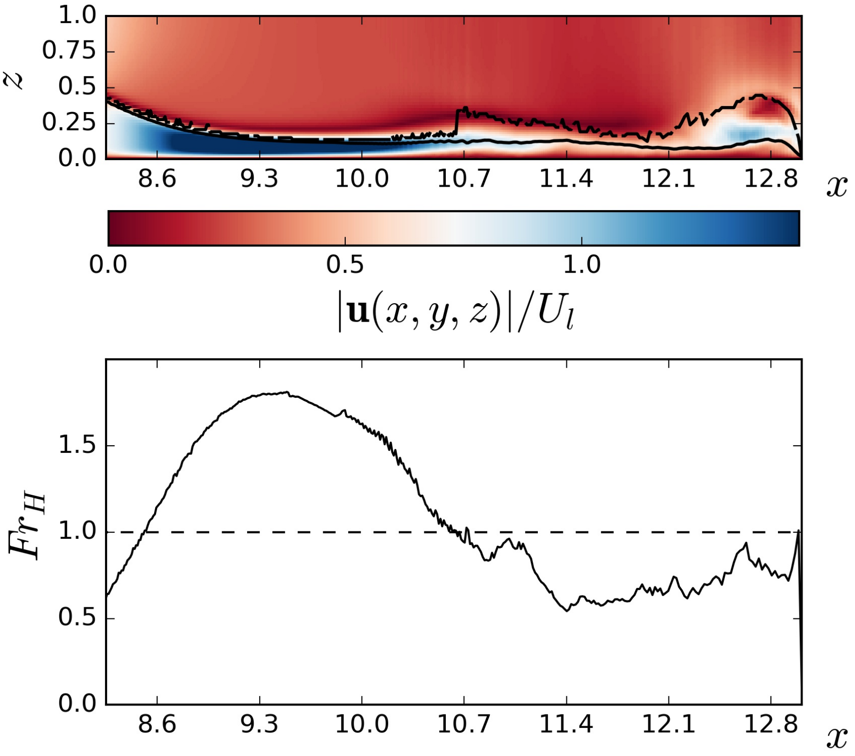

Figure 4.5: top: non dimensional radial velocity $\frac{|\bar{u}|}{U_l}$ on the mid-plane $y = y_0$; the continuos thick black line indicates the depth $h_l = \frac{\overline{g'h}}{g'}$ and the broken black line marks h_t, i.e. the interface $\rho = 3\%$, bottom: Froude number Fr_H vs. x. Case S3, $t = 16$.

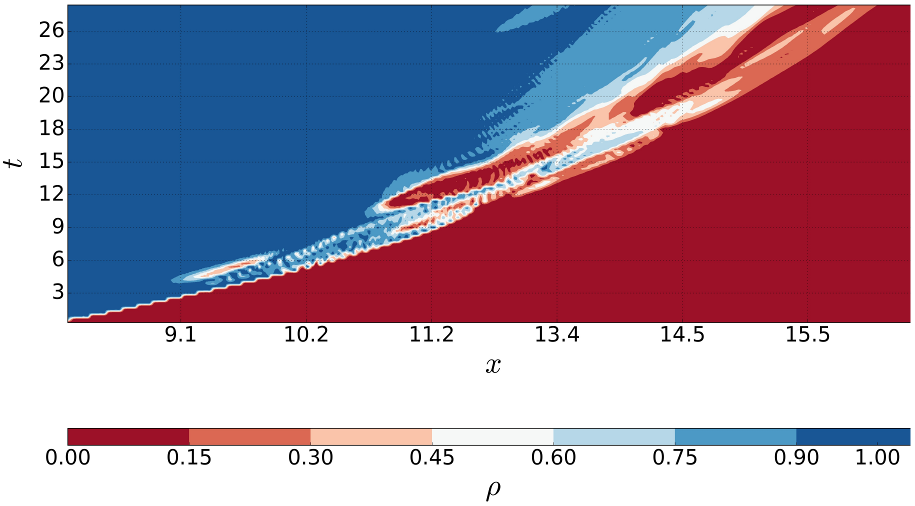

Figure 4.6: Hovmoller diagram, case S3, simulation $Gr = 2.0 \cdot 10^6$

current outside the spreading area at $x < 10.5$ (figure 4.5). Correspondingly, the Fr_H number is always sub-critical beyond the initial spreading area.

The analysis of the HD in figure 4.6 shows the evolution in time of the frontline, which is closely followed by a secondary, isolated, perturbation in the density field. Comparing this behaviour with the one in figure 4.1 it is clear that it represents the trace of an increased complexity in the structure of the head of the current, which is now composed of a ring of flow limited by two close frontal structures, one internal and the other at the external edge. This is consistent with the information provided by the evolution in time of the Froude number, figure 4.4 and 4.5.

The formation of isolated hydraulic shocks that follows the external front, bounding the head of the gravity current from the inside and the outside, is the distinctive feature of all the simulations up to $Gr = 8 \cdot 10^6$. It is also completely consistent with the solution of the theoretical model proposed by Garvine [1984]. At even larger values of Gr, starting from case S6 ($Gr = 2 \cdot 10^8$), the development of the current is dominated by the continuous production of alternating bands of fluid at different densities in the horizontal plane, i.e. 'rings'. These features are described in the next section.

4.2 High Grashof number

At sufficiently high inflow rates, alternating bands (or rings) can be observed in every horizontal section of the density and velocity fields. Rings appear

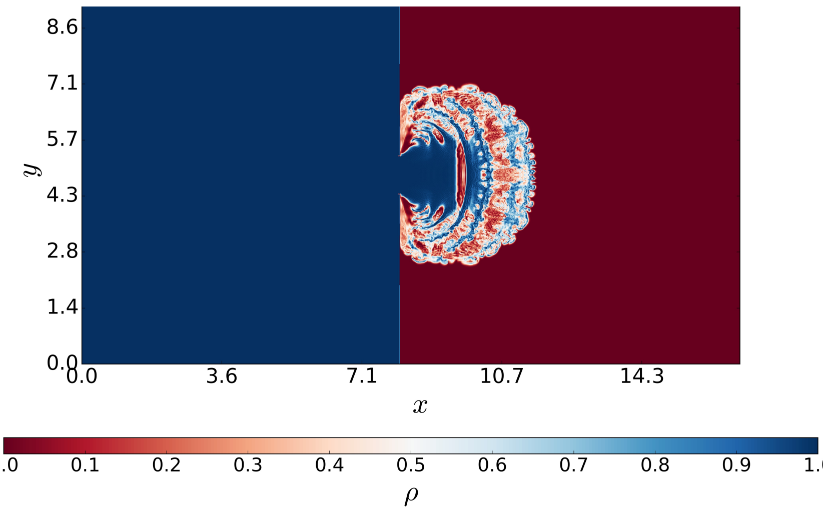

Figure 4.7: Density field on the horizontal plane at $z = 0.1$, $t = 8.7$, case S11

as axisymmetric, periodic structures (see, for example, figure 4.7 and figure 4.8), which persist during the entire simulation and extend mostly over a limited domain of the tank. They form at some distance from the symmetry axis and move inside the current as internal shocks. The rings maintain a type of self-identity for a variable (but relatively short) distance, after which they merge with each other and generally decay beyond a critical distance. In this range of Gr it is evident the deformation in the azimuthal direction of the axial symmetry of the vortex rings as they propagate outward. In particular it is visible a progressive disruption of the axial symmetry of the rings with the distance from the axis and the production of small scale vortical structures which are advected radially.

In the case of very high Grashof number, case S11, at $t = 8.7$, the position of the front is approximately at $x_f = 11.4$. Three internal ring structures are clearly visible both in the velocity field and the ρ field on the horizontal plane at $z = 0.1$ (shown in figure 4.7). The two rings closer to the origin are more regular and have higher velocities than the last one. The three ring structures visible in the horizontal plane section of the density field can easily be related to the axisymmetric bulges in the 3D view of the surface $\rho = 3\%$ (figure 4.9). Towards the origin of the current they emerge as small toroidal structures. These structures become larger and more prone to three-dimensional azimuthal instabilities as they approach the front. The map of $|\vec{u}|/U_s$ on the mid-plane $(x, y = y_0, z)$ shown in figure 4.11 highlights a series of three acceleration phases from high velocity, $Fr_H > 1 \rightarrow$ low velocity, $Fr_H < 1 \rightarrow$ high velocity, $Fr_H > 1$. The rapid variation in Fr_H (it decreases from close to $Fr_H = 1.6$ at $x = 9.6$ to a value of $Fr_H \sim 0.5$ at

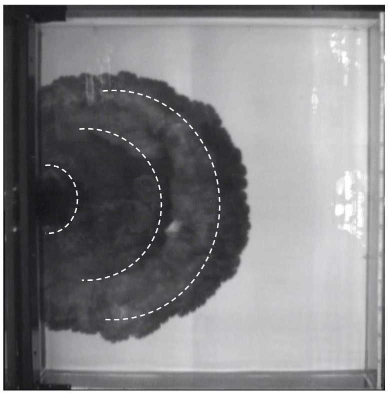

Figure 4.8: Top view image of the experiment S12, $t = 14.5$

x=10.0 in the considered case) is associated with an increase in the depth h_l of the current, marking the presence of a circular hydraulic jump. Similar behaviour is visible at $x = 10.4$ and $x = 11.0$. Corresponding to the high radial velocity regions before the jumps, at heights greater than the depth h_l, Kelvin-Helmoltz billows are responsible for the entrainment under the bulges visible in the profile of the h_t line in figure 4.11 and in the density isosurface shown in figure 4.7. Figure 4.10 shows in shades of grey the density contour at level $\psi = 3\%$ and in colour the velocity vectors on the meridian (x, z) plane at y_0, $t = 12$. The combined analysis of velocity field and density contour indicates the presence of rings associated with rapid variations in the radial fluid velocity field along x. The velocities are higher on the ascending side of the rings, similar to what is observed at the compressive part of the flow in the development of a shock wave in a volume of gas [Whitham, 1999]. Here, the velocity of the fluid is considerably higher than the phase velocity of the ring. Kelvin-Helmholtz billows, situated between the core of the current and the ambient fluid, hang above the position of the local maxima of velocity. There are two clearly defined rings in the region $8.9 < x_f < 1$ and a weaker third one that is close to $x_f = 11.4$. Beyond this position, the velocity is mostly radial and uniform up to the external front. As observed for $t = 8.7$, the bulges visible in the $\psi = \%$ surface correspond to zones of high radial velocity, and again, Kelvin-Helmoltz billows at the interface between current and ambient fluid are likely producing mixing.

Just before the end of the simulation S11, at $t = 16$, the planform occupy almost the entire surface of the tank. As expected, the depth of the current h_l is much more shallow than in the initial phase, there is only one circular hydraulic jump close to the symmetry axis and most of the flow has $Fr_H < 1$. Most of the Kelvin-Helmoltz billows have faded out, with the exception of the very active instability close to the jump, and the current propagates as a uniformly mixed flow of depth h_l.

The HD map in figure 4.14 clearly shows a succession of rings in the

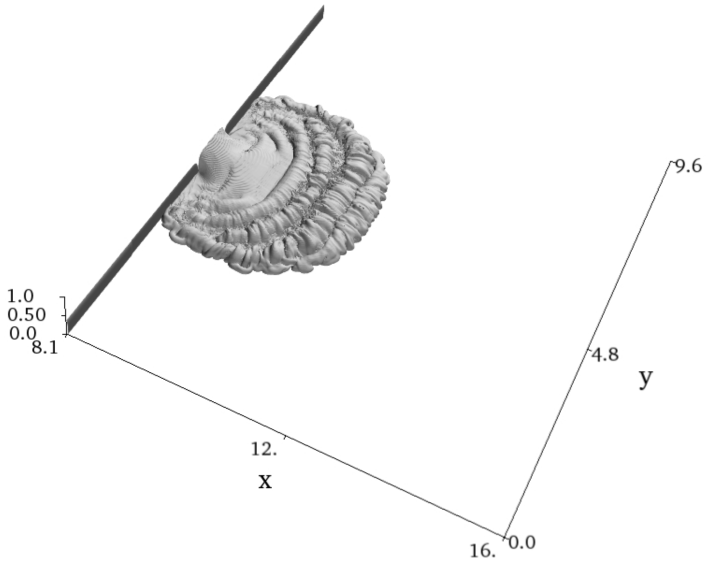
1.0
0.50
0.0
8.1
12.
x
16.
0.0
4.8
y
9.6

Figure 4.9: Case S11: $\rho = 3\%$ isosurface, $t = 8.7$

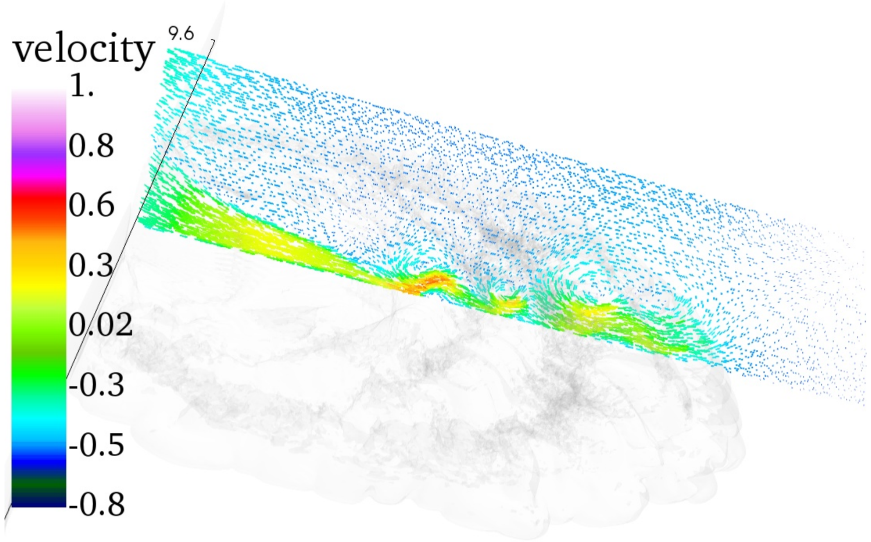
velocity
1.
0.8
0.6
0.3
0.02
-0.3
-0.5
-0.8
9.6

Figure 4.10: Case S11: velocity field on the mid-plane (x, z), $Gr = 8.1 \cdot 10^8$, $\epsilon = 0.03$, $t = 12$

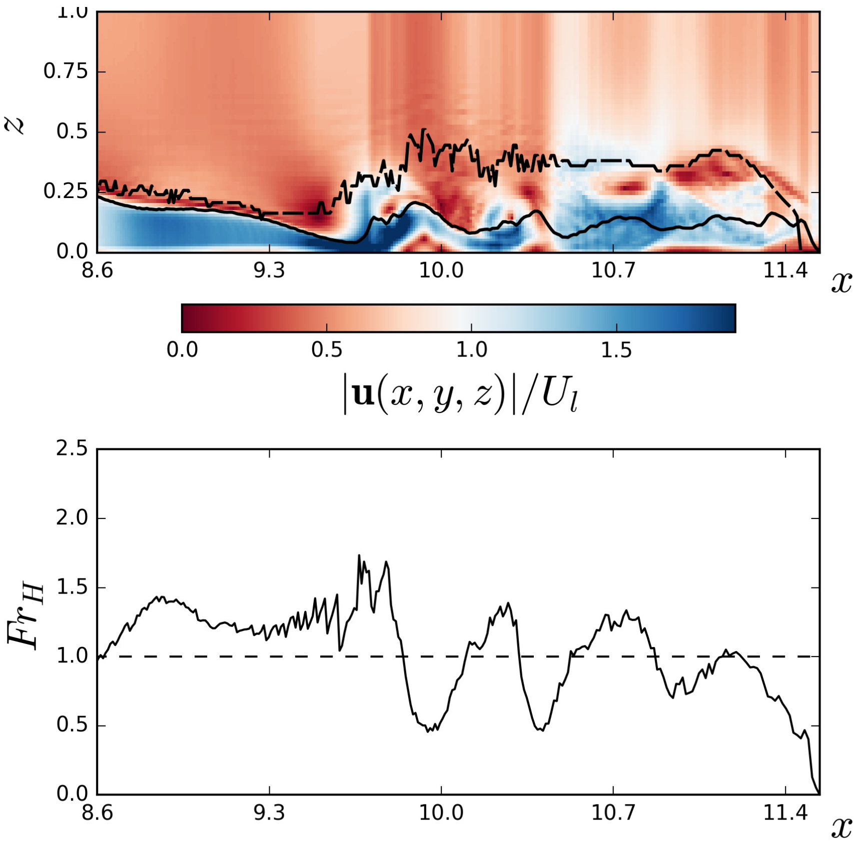

Figure 4.11: top: non dimensional velocity $\frac{|\bar{u}|}{U_l}$ on the mid-plane $y = y_0$; the thick black line indicates the depth $h_l = \frac{\sqrt{g'h}}{g'_0}$ and the thin line marks the interface $\rho = 3\%$; bottom: Froude number Fr_H vs. x ; case S11, $t = 8.7$

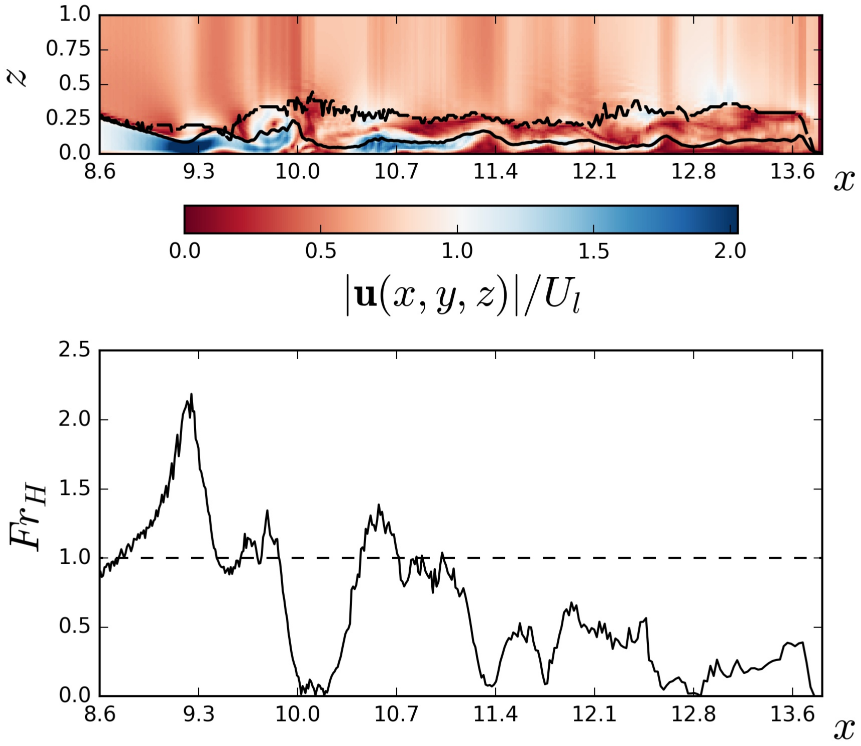

Figure 4.12: top: non dimensional velocity $\frac{|\bar{u}|}{U_l}$ on the mid-plane $y = y_0$; the black continuous line indicates the depth $h_l = \frac{\sqrt{g'h}}{g'_0}$ and the black broken line marks the interface $\rho = 3\%$; bottom: Froude number Fr_H vs. x ; case S11, $t = 16.0$

region $9 < x < 12$. A total of 11 rings are clearly identifiable during the available time.

The rings are continuously formed starting from $t = 3$ until the end of the simulation at $t = 22$, but beyond $x = 12$ the rings tend to merge and attenuate. The phase velocity of the rings is initially approximately 7 but decreases towards 4 after the formation of five rings, at approximately $t = 12.0$.

The recorded image frames of the experiment (such as the one shown in figure 4.8) can also be used to produce HD maps. Note that the experimental data are collected using a camera recording the top of the surface, whereas the salinity field used in the simulations is extracted at a carefully chosen level to obtain the best possible resolution of the structures. Moreover, note that the visibility of the rings in the experimental conditions depends on several external factors, such as the concentration of the dye, the depth of the current and the presence of disturbances on the free surface. In the experiment, rings are clearly detectable as alternating bands of different shades of grey due to the mixing associated with the hydraulic jumps. It is possible to verify from the HD (not shown) the presence of several rings. It appears that the rings have some periodicity; however, it is unclear whether the width of the rings is variable or whether some of them are too close to each other to be distinguished. The first small ring starts at approximately $t = 3$, and the rings are generated throughout the entire duration of the experiment in a variable area near the origin. Due to the presence of many light reflections from the dark surface of the current, it is unclear whether, after $t = 9$, the rings remain confined in a circle or whether they are able to propagate forward towards the external front in the final part of the spreading.

Most of the features illustrated in the simulated case S11 are also present in cases S6–S10.

The frequency of ring generation increases with ϵ, and the bulges visible in the $\psi = 3\%$ surface are less numerous but increasing in size at lower Gr. As an example, the number of rings observed for case S7 ($\epsilon = 0.010$) is close to 1/3 of the rings present in S11 ($\epsilon = 0.030$) in the same time period. The initial propagation velocity of the rings appears to vary between 5 and 0.5, but the HD method employed here is not accurate enough to properly investigate the evolution in time of the phase velocity. In fact, beyond a small initial distance, the phase velocity of the structures is difficult to evaluate as the shock structures evolve in a complex manner, often interacting with each other.

In all high Gr cases, the fluid velocity field and the evolution in time of the ring structures are related, as is the presence of Kelvin-Helmholtz billows over the local maxima of the fluid velocity in the ascending side of the rings. In the initial phase of spreading, close to the axis, rings are present in the entire volume of the current. As the current spreads out, the rings remain

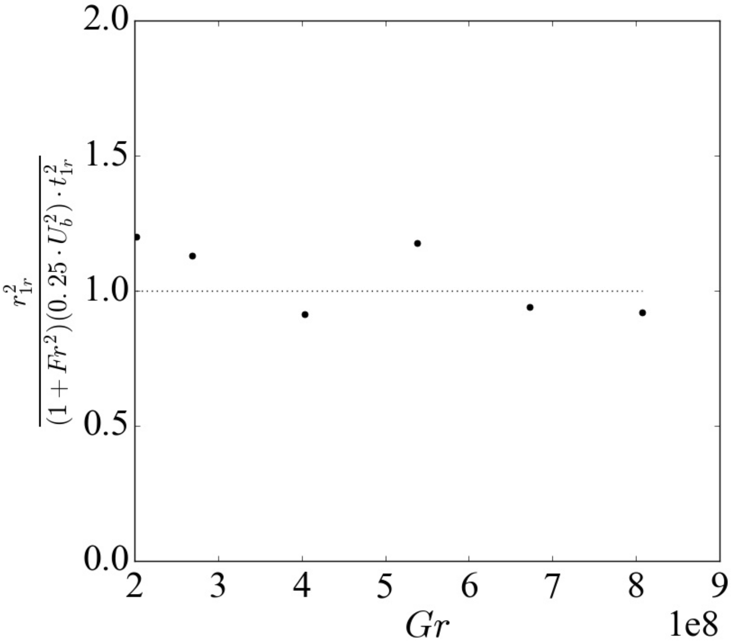

Figure 4.13: square of distance of the first ring from the symmetry axis (r_{1r}) with respect to the velocity times the travel time (t_{1r}) of the disturbance carried by the fastest gravity wave

mostly confined in the region $9.3 < x_f < 12.1$, leaving the fluid in the outer subcritical region $x_f > 12.2$ spreading radially in a uniform manner.

Looking carefully at all the Hoevmoller diagrams it seems that the position of the first ring tends to be the closest to the axis of symmetry, the position of the successive rings are gradually shifted outward. The time of formation of the first ring depends on ϵ and is subsequent to the time t_0 of formation of the axisymmetric current. The radial position of the first ring is related to the time it takes the fastest gravity wave to travel the distance r_{1r} from the axis of symmetry to the position of the hydraulic jump. As shown in figure 4.13, in all cases the position of the jump approximately corresponds to the time it takes to a gravity wave with velocity $U_b = \frac{1}{4}U_s$ to cover r_{1r}. Clearly, as U_b is evaluated with respect to the velocity of the fluid, the velocity with respect to an observer at rest is $(1 + Fr_H^2)U_b^2$. The value of Fr_H^2 is obtained from $Fr_H(x)$ near the position of the jump at a time close to the formation of the jump and does not depend on U_s since it is evaluated as in Shin et al. [2004]. The time interval t_{1r} is the time of formation of the first shock determined from the HD with respect to the starting time of the perturbation, visible from the $Fr_H(x)$ after the propagation of the external front. U_b is slower than U_s because U_s^2 is defined in terms of $g'H$, which is clearly an overestimate of the maximum velocity of

	R_r^2	$1+Fr^2$	t_r^2
S6	4.0	3.2	1.2
S7	2.5	2.2	0.8
S8	2.5	2.7	1.0
S9	2.7	3.2	1.0
S10	4.8	5.0	1.0
S11	4.0	2.6	1.2

Table 4.1: R_r^2 square of distance of the first ring from the symmetry axis, t_r^2 time of propagation of the wave with velocity U_b

the gravity waves, since their depth is always less than $H/2$. In fact, the effective velocity $U_b = \sqrt{\frac{g'H}{4}} = \sqrt{g'h_e}$ can be related to a current having effective depth $h_e = H/4$, which is consistent with the value of h_l of the current at the time and position of the jump. If the time of formation of the first ring is scaled using $T_s^* = \frac{H}{U_b}$, then the non dimensional relation $R_r^2 = (1+Fr^2) \cdot t_r^2$ approximately holds, as expected. In table 4.1 are listed the values of $R_r^2 = (\frac{r_{1r}}{H})^2$, square of the distance of the first ring from the symmetry axis, the factor $1+Fr^2$ and the non dimensional time $t_r^2 = \frac{t_{1r}}{T_s^*}$.

The HD of S13 (extended domain case), shown in figure 4.15, reveals some more features about the propagation of rings, which appear only at large times. The most evident aspect is that only few rings (approximately 1 out of 10) are able to escape from the confining area, and only two of them actually reach the external front. This spatial pattern can also be clearly identified by examining the horizontal section of the density field $\rho(x, y, z_c)$ at the final stage of spreading for $t = 65$ (figure 4.16). The first ring reaching the front is generated at approximately $t = 17$ and meets the front at approximately $t = 41$, indicating that the average phase speed of the ring is close to twice the average velocity of the frontline. The other feature is that rings are produced continuously in the entire 50 s of simulation, i.e. up to $t = 60$.

The frequency of ring generation, defined as the number of rings generated in the total time of simulation divided by the total time, χ, is related to the inflow Q. The linear least squares fit indicates a possible functional relationship $\chi = \beta Q^\gamma$ with $\beta = e^\alpha$ m^{-3}. The regression coefficients are $\alpha = (6.577 \pm 1.024)$ and $\gamma = (0.9635 \pm 0.139)$, and the squared Pearson correlation coefficient is $\mathcal{R}^2 = 0.913$. Unfortunately, the error associated with the determination of the exponent γ is large, and the confidence interval at the 95% level of probability is in the range $[0.68-1.24]$. The non-dimensional frequency of ring generation $\eta = \chi T_s = \chi H/U_s$, shown in figure 4.17, is relatively constant over the range of Gr considered in the study. The average

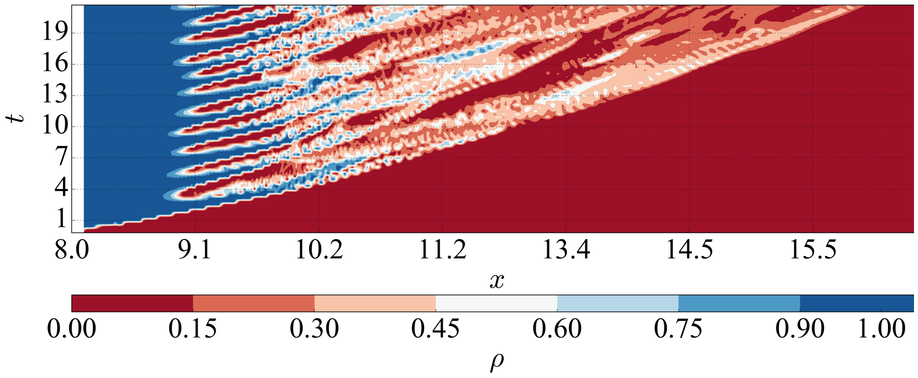

Figure 4.14: Hovmoller diagram case S11, simulation $Gr = 8.1 \cdot 10^8$

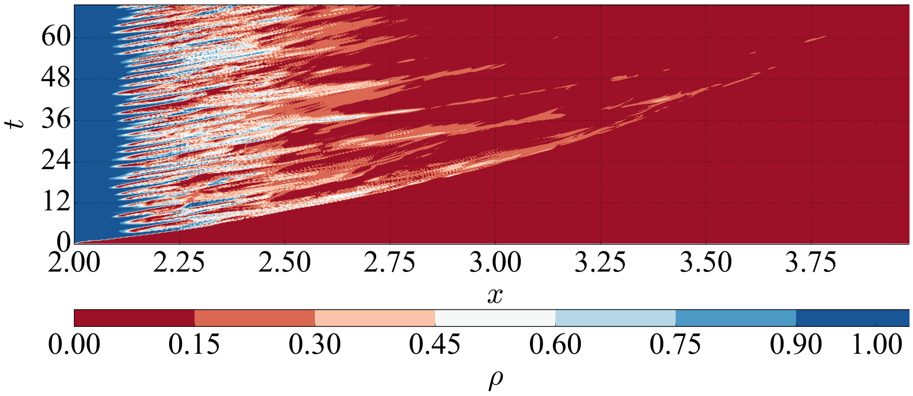

Figure 4.15: Hovmoller diagram case S13, simulation $Gr = 5.4 \cdot 10^8$

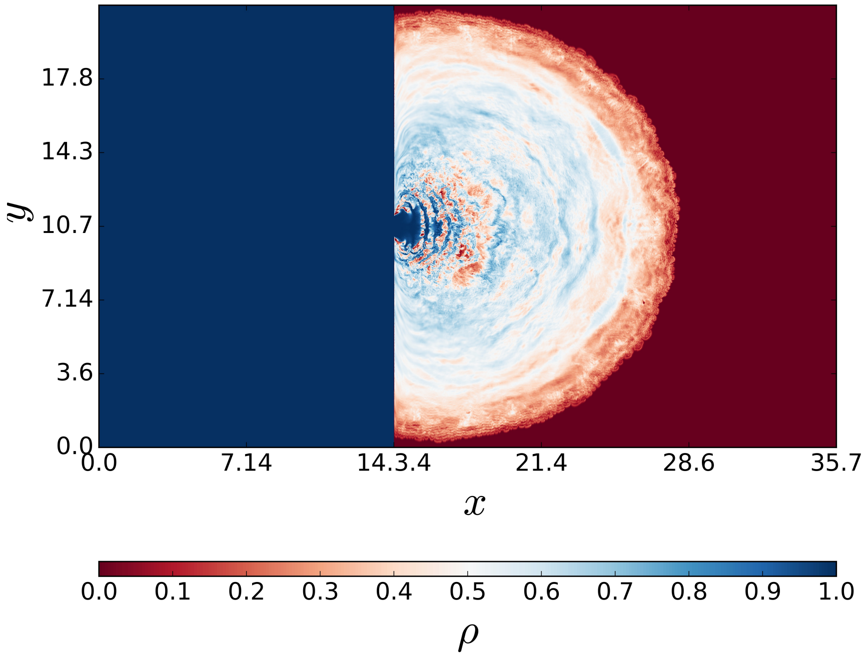

Figure 4.16: Case S13: $\rho(x, y, z_c)$, $t = 64$, case S13

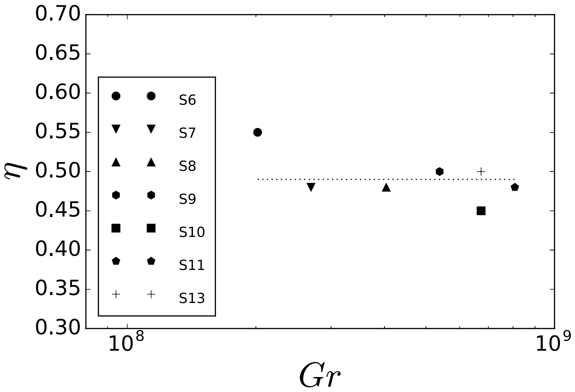

Figure 4.17: Dimensionless frequency of ring generation η vs. Gr; dots represent S6-S11; cross is S13; dashed line indicates $\bar{\eta}$

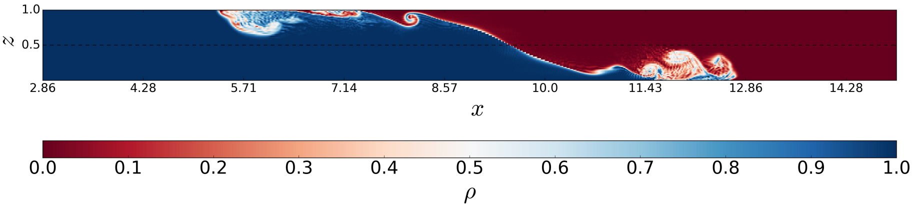

Figure 4.18: ρ on the meridian plane at $y = y_0$, $t = 8.2$, case S10

value is

$$\bar{\eta} = 0.48 \pm 0.06, \tag{4.1}$$

with the error being evaluated as the confidence interval around $\bar{\eta}$ at the 95% level of probability.

The estimate of η relative to S13 (indicated by a cross in figure 4.17) is evaluated on a time period that is five times longer than the duration of the other cases. Some similarity between the results obtained by Maxworthy [1980] for the frequency of generation of ring-like solitary waves produced by collapsing volumes of fluids, propagating in a stratified ambient fluid, and the present results (e.g. see plates 7 and 8 in the original paper) is devisable. In both cases, the number of ring-shaped structures depends on the Grashof number in the same way, but in the former, the solitary waves move in the stratified fluid externally to the generating gravity current, whereas in the latter, the rings are embedded in the current propagating in a homogeneous environment. Moreover, the rings discussed here have the structure of hydrodynamic shocks and are related to a three-dimensional, intrinsically hyperbolic nonlinear problem, whereas the solitary waves described in Maxworthy [1980] are nonlinear dispersive waves moving along the interface between two shallow layers of a stratified fluid.

4.3 The reverse current

As mentioned at the beginning of the section, it is typical of lock-exchange flows that a current of positively buoyant fluid flows in reverse direction in the upper level of the lock volume. The problem of the reverse current is not investigated here mainly for two reasons. The first is that from the experiments of Thorpe and Kavcic [2008] about circular internal jumps it is expected that a cylindric current moving over a denser fluid would show a more turbulent and complex dynamics. The second reason is that we do not have (yet) experiments with measurements of the frontal propagation in the dense fluid, so we cannot compare the results. That said, a preliminary analysis may help indicating qualitatively the main features of the reverse

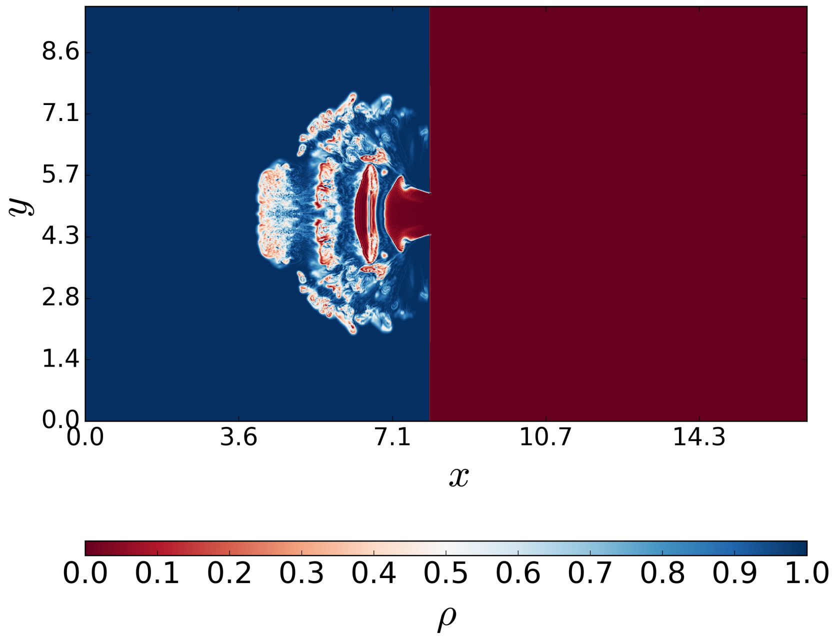

Figure 4.19: ρ on the horizontal plane at $z = H - 0.2$, $t = 8.2$, case S10

current. Figure 4.18 shows the density field on the meridian $y = y_0$ plane for a high Gr case, S10 at t=8.2. The image can be compared with figure 4.19, illustrating the section of the density field on an horizontal plane close to the top of the tank, at $z = H - z_b$, showing the spreading of the light current propagating in the lock volume. The current acquires an axial symmetry and there are shocks which are almost periodically produced in the flow. The reverse current has a spreading slightly faster than the current propagating on the bottom, it seems that the revere shocks have a less pronounced curvature than the ones on the bottom, resembling more a 'bar' than a 'ring'. Compared with the features shown in figure 4.7 for the similar case S11, the reverse current appears to have a less stable structure and is more irregular.

At a later time, before the current hits the lateral bottom, figure 4.20 shows the density field on the meridian $y = y_0$ plane and figure 4.21 the section of the density field on an horizontal plane close to the top of the tank. Here the difference in the propagation velocity between top and bottom currents is apparent. Also in this case it is seen that the axis of symmetry moves slowly along the line $y = y_0$ in the meridian plane, but the axial symmetry of the flow appears less definite, as if the plane parallel component

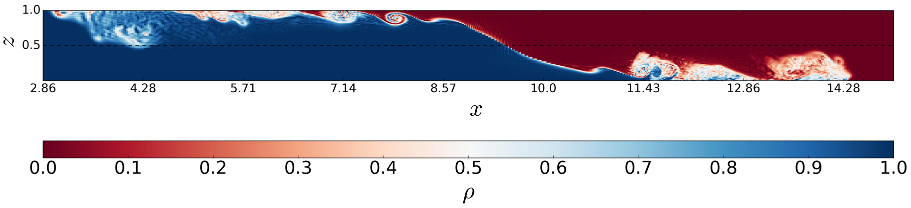

Figure 4.20: ρ on the meridian plane at $y = y_0$, $t = 13.5$, case S10

of the flow had a more pronounced role in determining the general feature of the current than the equivalent in the bottom current.

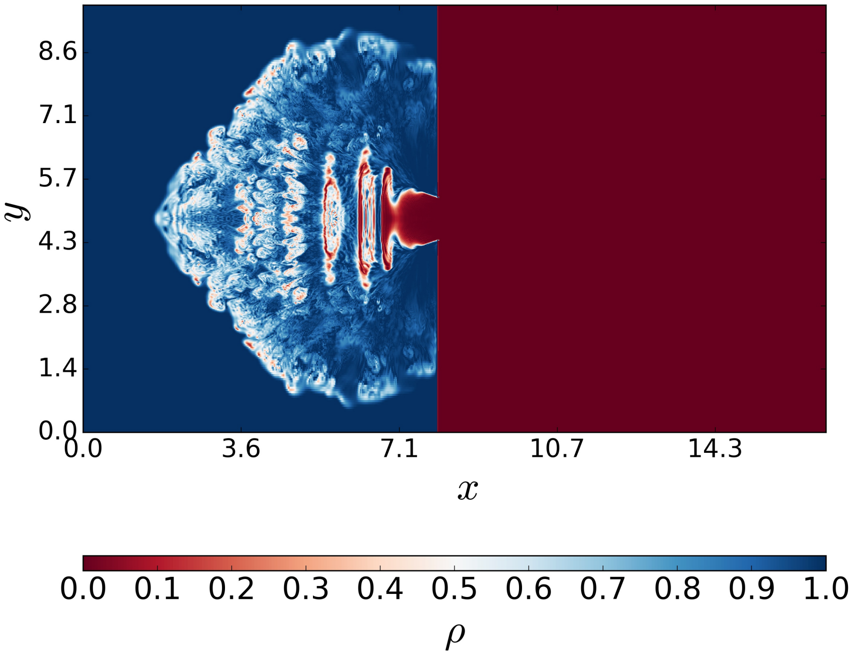

Figure 4.21: ρ on the horizontal plane at $z = H - 0.2$, $t = 13.5$, case S11

Chapter 5

Spreading regimes for axisymmetric, constant volume flow gravity currents

5.1 Dimensional analysis and asymptotic solutions

The existence of characteristic frontal spreading regimes governed by the dynamical balance of some of the terms in the shallow water equations was suggested by Fay [1969] and successively by Hoult [1972] and Huppert and Simpson [1980]. The idea is that, for dimensional reasons, the inertial term in the momentum equation prevails among the various opposing forces in the initial part of the spreading (the inertial-buoyancy equilibrium regime), while the surface tension at the interface dominates the very end of the process in liquid-air systems. The balance between the buoyancy and the inertial term, assuming the flow hydrostatic and axial symmetric, can be expressed as

$$(\rho_1 - \rho_2)gh^2 \cdot \pi r = \rho_1 \pi r^2 h \ddot{r} \tag{5.1}$$

which, by using the volume conservation

$$Qt = \pi r^2 h, \tag{5.2}$$

can be expressed as

$$\frac{\ddot{r}}{g'} = \frac{Qt}{\pi r^3}. \tag{5.3}$$

As in the preceding sections Q is the volume flux of dense fluid. In case of negligible mixing the volume of the cylindrical current is assumed equal to Qt. In one-layer flows the effects of viscosity are the leading term at intermediate times, i.e. in the viscous-buoyancy equilibrium regime [Didden and Maxworthy, 1982, Huppert, 1982], i.e. when time is too short for the spreading to fall in the ultimate surface tension regime, but it is too long to be in the inertial regime. The surface tension regime does not appear in two-layers flows as is the case at hand. In this case the balance in the viscous-buoyancy regime is given by

$$(\rho_1 - \rho_2)gh^2 \cdot \pi r = \rho_1 \frac{\nu \pi r^2 u_r}{h}. \tag{5.4}$$

i.e.

$$u_r \cdot \frac{\nu}{g' h^2} = \frac{h}{r} \tag{5.5}$$

Starting from the elementary dimensional analysis of the balance equations, by substituting h from 5.2, in (5.3) and (5.5), the asymptotic expression for $r(t)$ is obtained respectively as

$$r(t) \propto (g'Q)^{1/4} t^{\frac{3}{4}} \tag{5.6}$$

during the inertial-buoyancy regime and

$$r(t) \propto (\frac{g'Q^3}{\nu})^{1/8} t^{\frac{1}{2}} \tag{5.7}$$

during the viscous-buoyancy regime. The concept of asymptotic regime of spreading has been applied by several authors in the past [see Chen, 1980, for an exhaustive literature review], e.g. to assess the spreading of oil by a constant-volume spill at sea [see e.g. Hoult, 1972, Huppert and Simpson, 1980]. The presence of the two equilibrium regimes was observed by Britter [1979] in a series of experiments reproducing negatively buoyant axisymmetric currents running on a rigid bottom. Unfortunately, the analytical solution to the constant-inflow initial value problem in the inertial-buoyancy equilibrium has proven to be most elusive. Britter [1979] was not able to find an exact analytical solution of the self-similar problem, i.e. the coupled system of non-linear ordinary differential equations. Opposite approaches were pursued by Chen [1980] and Garvine [1984]; the former attempted to numerically solve the similarity problem in the inertial-buoyancy regime, i.e. integrating backward in time the self-similar ordinary differential equations from the final position of the front, and the latter solved the initial value problem in the spirit of Penney and Thornhill [1952] and Abbott and Hayashi [1967], following the method of analysis of the characteristics. It was soon found that the time rates of spreading found in the self-similar solution proposed by Chen [1980], $r \propto t^{3/4}$, cannot be considered as the asymptotical regime reached by the solution of the initial problem studied by Garvine [1984], $r \propto t^{0.92}$, due to the completely different spreading rates.

Grundy and Rottman [1986], using the phase-plane method of Sedov [1993], demonstrated that no continuous analytical similarity solution satisfying the boundary conditions on the axis of symmetry can exist for the general time-varying-inflow axisymmetric initial value problem, except in the case of constant-volume release. In fact, they demonstrated that the numerical solution of Chen [1980] was not compatible with the boundary conditions of the original problem. In the case of currents with a variable flow rate but planar symmetry, Gratton and Vigo [1994] found that up to four different families of solutions can exist, only one of which is continuous. This result led Bonnecaze et al. [1995] to suggest that in the case of a constant flow rate, given the non-linear, hyperbolic nature of the flow, the absence of continuous solutions might imply that only discontinuous solutions with shocks could eventually be found. As mentioned in the introduction, there is currently no accepted theory about the initial spreading regimes for constant-flow-rate, axisymmetric gravity currents; specifically, there are contrasting views about the possible asymptotical spreading regimes obtained from elementary scaling considerations and as a solution of the initial value problem.

The existence of an additional regime, the 'slumping phase', was proposed by Huppert and Simpson [1980]. The slumping, which dominates the short times prior to the onset of the inertial-buoyancy equilibrium, has been investigated by several authors, e.g. Ungarish and Zemach [2005], in the limited context of planar and fixed-volume axisymmetric gravity currents. The presence of a slumping phase in constant-flow-rate, axisymmetric gravity currents has not yet been given proper attention, probably due to the uncertainties already found in the theoretical assessment of the inertial-buoyancy regime. Its presence, however, might justify the inconsistency between the 'spreading regime' introduced by Garvine [1984] and the solution found by Chen [1980] as part of the asymptotic solution of the initial value problem.

The geometry of the problem here considered is slightly different from that used in the formulation of the slumping theory. In fact, the box model of Huppert and Simpson [1980] is based on two conditions: the first is that in the slumping regime, the current conserves the volume, i.e. the volume of the current at any time is the same as the cylindrical initial volume of the denser fluid; the second is that the Froude number at the front of the current can be expressed as a monotonic function of the fractional height $\phi = h/H$ of the depth of the current h divided by the total depth of the fluid H. The functional relationship is based on the experiments at a constant flow rate of Simpson and Britter [1979].

The extension of the original slumping concept to the constant-flow-rate problem can be simply obtained by replacing the condition of fixed volume with a condition in which the volume increases in time at a fixed rate. The result is not as simple as the constant velocity law found for planar and axisymmetric constant-volume gravity currents. In the present case, it is found that

$$r^{4/3} - r_0^{4/3} \propto C_{sl} t^{7/6} \tag{5.8}$$

where

$$C_{sl} = \left(\frac{g'^3 Q H^2}{\pi} \right)^{1/6} . \tag{5.9}$$

The time after which the current exits the slumping regime can be evaluated as

$$t_i = \frac{aQ}{\pi g' H^2} \tag{5.10}$$

where $a = \left(7/4\ \phi_0^{-2/3}\right)^2$ is a numerical coefficient.
The details of the calculations are presented in appendix B.

5.2 Evaluation of the regimes

To investigate the spreading regimes obtained in our simulation and to check whether they fit the theoretical expressions, the radial spreading rates obtained in the simulations are evaluated and compared with the expected ones. The position of the external front is obtained from the non-dimensional density field $\rho(x, y, z_b, t)$ provided by the numerical simulations with the frequency of the numerical output being 5.0 s^{-1}. The filtering procedure applied to remove the effects of lobes and clefts provides a decomposition of the frontline kinematics in a radial spreading $R(t)$ about a centre of symmetry $(x_c(t), y_0)$ that translates in time along x. The statistical analysis is successively applied on the series of radial positions about the symmetry axis, $R(t)$.

The time series $R(t)$ are subdivided into three different time intervals separated by the transition times corresponding to the onset of the inertial regime and the beginning of the viscous phase. The sub-series are then compared with the asymptotical expressions expected for the slumping, inertial and viscous phases. In the case of the onset of the viscous-buoyancy regime, a simple similarity scaling provides a reasonable first guess of the time beyond which viscosity-buoyancy equilibrium holds, $t_v = (\frac{Q}{\nu g'})^{1/2}$ [Britter, 1979]. For the onset of the inertial-buoyancy regime, the time estimate (5.10) is a starting point reference for finding the beginning of the inertial-buoyancy regime. As discussed in section 2.2, data corresponding to times $\frac{t}{t_0} < 1$, i.e. when the inflow was not yet stabilised, are discarded from the analysis. The actual transition times are determined from the initial guesses by determining the best fit interval for each regime. The estimated times of transition t_0, t_i and t_v are listed in table 2.2 together with the total duration of each test case. It can easily be verified that only the cases at lower Grashof numbers are expected to enter the viscous phase. In high Gr cases, i.e. S6–S11, the duration of the simulation is not expected to last long enough to approach the conditions of asymptotical spreading for the inertial regime described in the literature. This is the reason for why case

	t'_s	t'_i	t'_v	R'_s	R'_i
S1	4.9	5.8	8.7	1.21	1.36
S2	4.6	5.5	11.9	1.21	1.43
S3	4.3	5.5	16.2	1.21	1.50
S4	4.6	5.5	18.8	1.28	1.43
S5	3.2	4.1	22.9	0.93	1.21
S6	2.9	4.9	20.9	1.07	1.43
S7	3.3	3.5	13.1	0.86	1.14
S8	3.1	4.5	14.8	0.93	1.36
S9	3.1	5.4	17.3	0.93	1.57
S10	2.9	5.8	20.4	1.07	1.71
S11	2.9	5.5	19.4	1.00	1.64
S12	3.3	5.4	16.4	1.11	1.64
S13	3.1	5.2	57.3	0.93	1.57

Table 5.1: 'Best' transition times and corresponding front positions estimated from the statistical evaluation of the time series.

S13 has been set up on an extended domain. To summarise, the expressions considered in the statistical fitting procedure are as follows [see section 5.1 and Britter, 1979]:

$$R_1^{4/3} = a_f + b_f \cdot t^{7/6} \tag{5.11}$$

$$R_2 = c_f + d_f \cdot t^{3/4} \tag{5.12}$$

$$R_3 = e_f + g_f \cdot \sqrt{t} \tag{5.13}$$

for the slumping, inertial-buoyancy and viscous-buoyancy regimes, respectively. The coefficients a_f, c_f and e_f are introduced because there is no abrupt transition from one phase to the subsequent phase; thus, even if the transition times t_i and t_v represent the 'best' subdivision for the series to follow the theoretical laws, the starting point regime is individuated at some small distance from the radius corresponding to the transition time. This choice allows all points to be retained in the analysis, thereby avoiding the need to exclude the transition periods.

On each time interval, the series $R_i(t)$, $i = 1,\ 2,\ 3$, are processed through a standard least squares regression analysis and fitted to the corresponding analytical expression. The first interval considered is the time period $t'_i - t'_s$ in which the $R_1(t)$ is expressed by (5.11), i.e. it is in the slumping regime. The second interval $t'_v - t'_i$ is where the front position $R_2(t)$ follows (5.12), i.e. where the current is in the buoyancy-inertial equilibrium. The transition times t'_s, t'_i, t'_v in table 5.1 may be compared with the expected values t_i, t_v and the time of stabilisation of the volume flow at the gate t_0 in table 2.2. t'_s is the time used as a lower bound of the slumping phase.

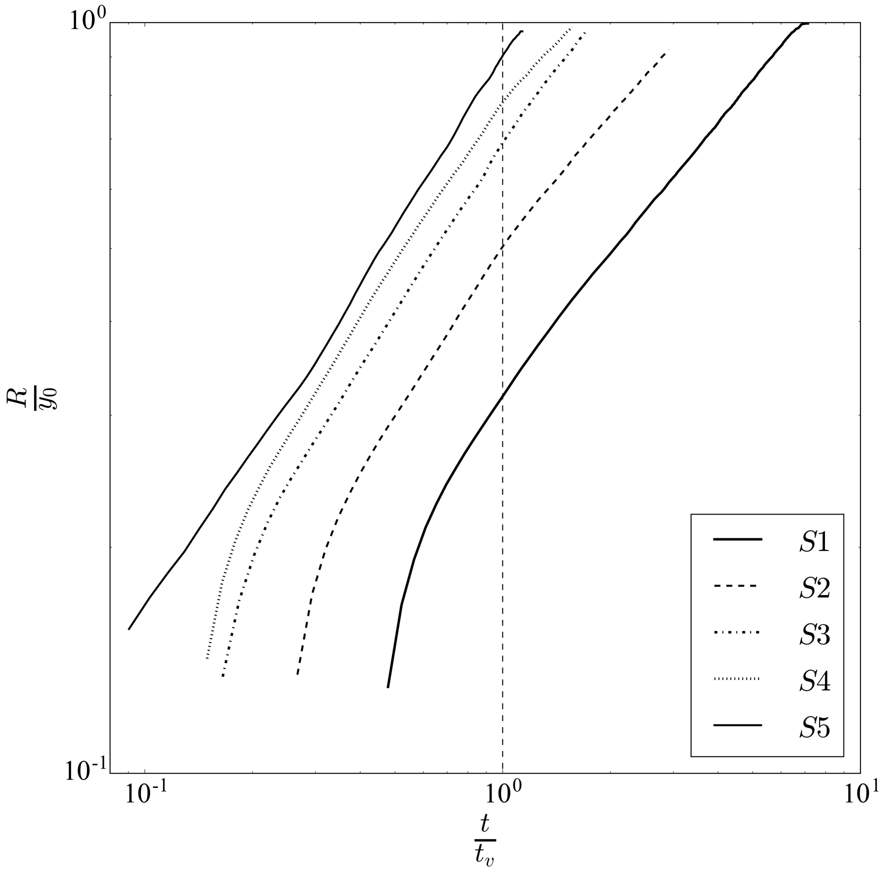

Figure 5.1: Non-dimensional front position vs. non-dimensional time. The vertical dashed line at $t/t_v = 1$ represents the transition to the viscous phase. Cases S1–S5: low Grashof number

The comparison of R_i' in table 5.1 with r_r from table 4.1 shows that in all cases S6–S11, the position of the first ring is just after R_i', i.e. at the beginning of the inertial regime.

The time evolution of the radial front position for the entire duration of the simulations is investigated herein. The cases at low Grashof numbers (cases S1–S5) are plotted in figure 5.1, the adopted scaling highlights the transition between the inertial phase and the viscous one. In these cases, it is clearly observed that the gravity currents do enter the buoyancy-viscous equilibrium regime, although the duration of the buoyancy-inertial equilibrium regime increases at the expense of the viscous phase with increasing Gr. Within this range of Gr values, $[10^4$–$10^6]$, the slumping phase hardly appears (as discussed later).

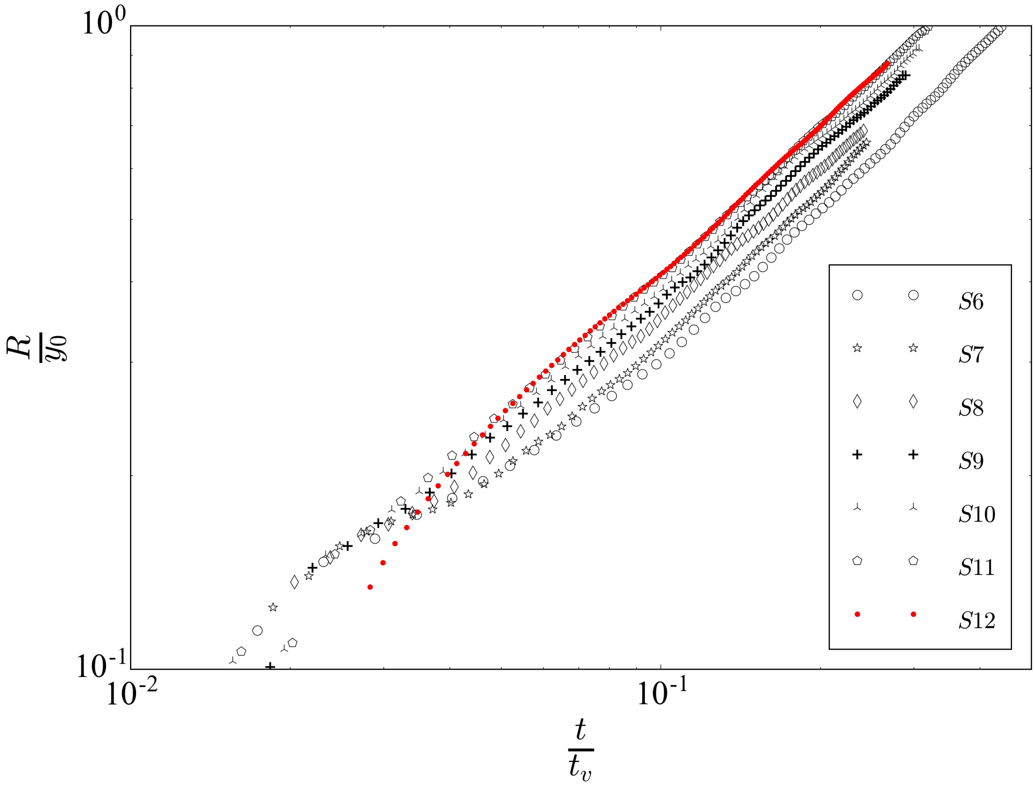

Figure 5.2: Non-dimensional front position vs. non-dimensional time cases S6÷S11: high Grashof number; red dots are experimental data from S12

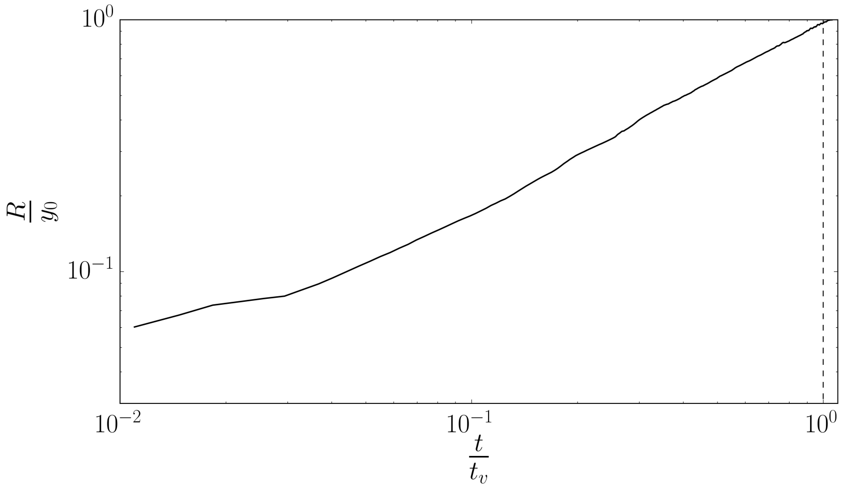

Figure 5.3: Case S13 extended domain ED; non-dimensional front position vs. non-dimensional time. The vertical dashed line at $t/t_v = 1$ represents the transition to the viscous phase. High-frequency oscillations at $t/t_v > 1$ are a border effect.

The time evolution of the currents at medium-large Gr (simulations S6–S11 and experimental data S12) is presented in figure 5.2, where time is made non-dimensional with t_v. Note that in these cases, the currents do not develop enough to enter the viscous phase. This is the reason why if the scale t_i were used, all the radial front time evolutions would collapse over a single line. All lines are parallel in the inertial-buoyancy domain. The series S11 and S12 are very close, indicating a good correspondence between experiment and numerical simulation. An inspection reveals that the two series show signs of a small-amplitude, large-scale oscillation due to the interactions between rings and the external front.

Note that t_v increases with Gr; consequently, the part of the inertial phase described by the simulation progressively decreases due to the finite dimension of the domain LD. The results of the spreading in the extended domain ED, i.e. case S13, are illustrated in figure 5.3. Here, the position of $t/t_v = 1$ indicates that the inertial phase is completely covered by the simulation. It is possible to observe that in the long period, the radial spreading is close to the asymptotic regime and that the perturbations in the data become less oscillatory as the inertial phase develops towards the viscous transition. The high-frequency noise at the end of the simulation is the effect of the wall proximity.

5.3 Slumping phase

The squared Pearson correlation coefficient $\mathcal{R}^2$ is approximately 1.00 for all cases considered, indicating that the regression analysis in each numerical simulation (5.11) closely follows the proposed asymptotic expression for the slumping regime (5.8). In figure 5.4, the presence of a slumping phase is visible to the left of the vertical dashed line $t/t_i = 1$. All points collapse towards the horizontal line at $\frac{R^{4/3}}{a_f+b_f t^{7/6}} = 1$ in the slumping region, where a_f is found to be very small in all cases.

To relate b_f to the parameter C_{sl} in (5.8), the ratio between the value of the statistical estimate b_f and the coefficient of the asymptotic law C_{sl} is shown in figure 5.5. The average of the points, i.e. $\bar{\mu} = < \frac{b_f}{C_{sl}} >$, is indicated as a dashed line. A single star indicates the value of $\bar{b}_{fexp}$, where b_f is calculated using the data from experiment $S12$, and it is normalised with the scale of $S11$, which is the closest numerical simulation. The box model (5.8) is found to be in reasonable agreement with (5.11), where $\bar{b_f} = \bar{\mu} C_{sl}$, and $\bar{\mu} = (0.37 \pm 0.05)$. The error is taken as the statistical error at the 95% confidence level. The expression of the front position with time in the slumping regime would then be expressed as

$$r(t)^{4/3} = \bar{\mu} C_{sl}\ t^{7/6} \tag{5.14}$$

Cases S1 and S2 have been excluded due to the very short duration of the phase. Comparing the duration of the phase obtained from figure 5.4 with the differences $t_i - t_0$ (see table 2.2), it is apparent that in the three cases (S7, S8, and S9/S13) where the duration is longer, the slumping phase starts before the flow rate at the gate Q stabilises. In some other cases (S4, S5, S6, and S11), the slumping starts at approximately t_0. The remaining cases, S1, S2, and S3, are the cases with the shortest slumping duration.

5.4 Inertial-buoyancy equilibrium phase

The presence of an inertial-buoyancy equilibrium phase following (5.12) and corresponding to the similarity expression (5.6) is observed in all cases, with a very high value of the Pearson correlation coefficient ($\mathcal{R}^2$ exceeding 0.997) found in all regressions used for estimating d_f. In figure 5.6, the inertial regime appears as a region with a constant value of the non-dimensional front position $R/(c_f + d_f t^{3/4})$ vs. non-dimensional time t/t_i. Again, since $c_f \ll d_f$ in all cases, the value of the ordinate corresponding to the dashed horizontal line indicates the coefficient k_s in

$$r = k_s d_f t^{3/4}. \tag{5.15}$$

The estimated value is

$$\kappa_s = (2.4 \pm 0.1) \tag{5.16}$$

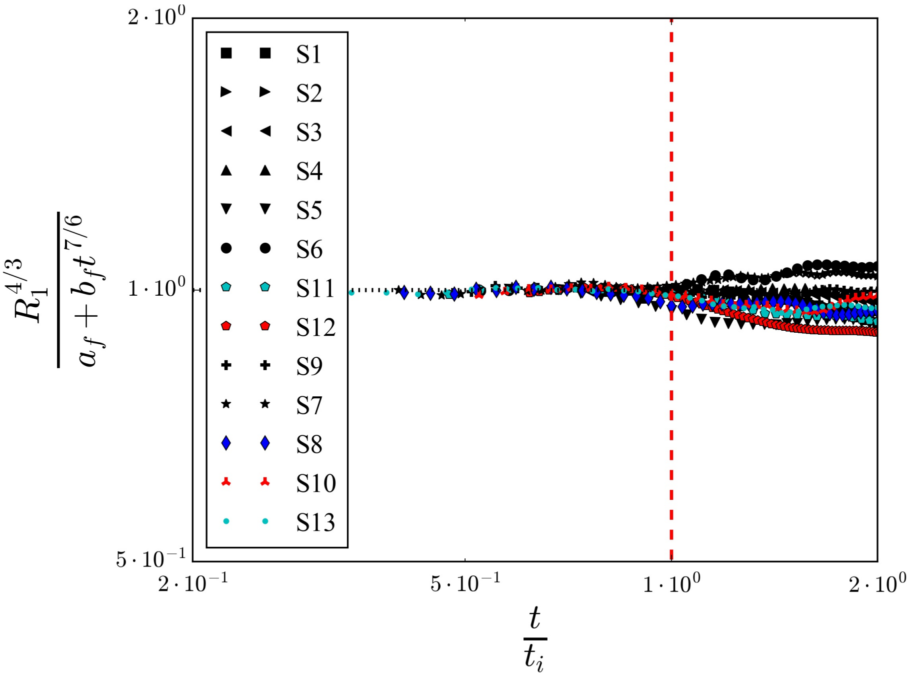

Figure 5.4: Domain of existence of the slumping regime (5.11), non-dimensional radial position vs. non-dimensional time. Vertical dashed line indicates the expected transition from the slumping phase to the inertial phase

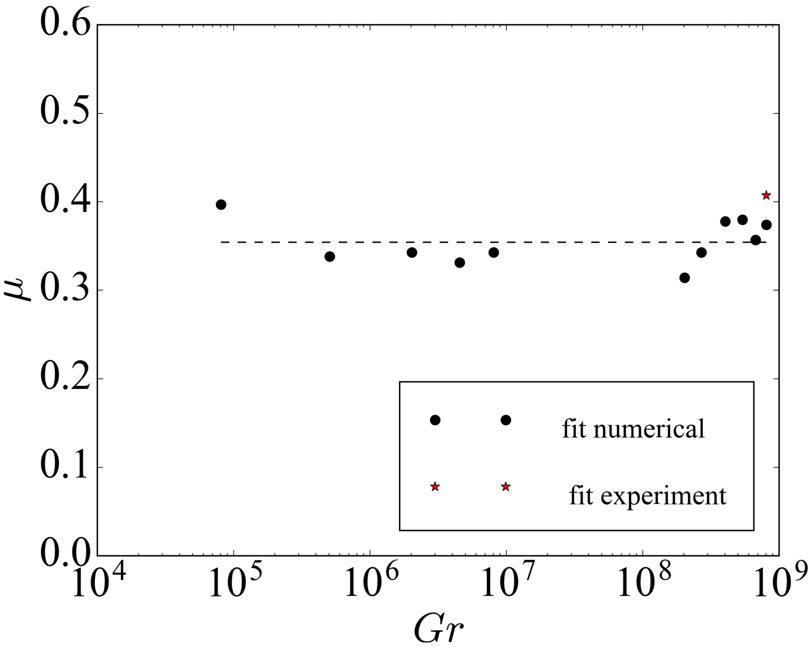

Figure 5.5: Non-dimensional coefficient b_f normalised by C_{sl} (5.11) vs. Gr, cases S1–S11. Dashed line represents $\bar{\mu} =< \frac{b_f}{C_{sl}} >$

where the error indicates the band of values between which all points are bounded in the inertial regime area to the right of $t/t_i = 1$. The inertial parameter d_f can be related to C_{in} in (5.12), considering the non-dimensional parameter $\delta = \frac{d_f}{C_{in}}$ where

$$C_{in} = (g'Q)^{1/4}. \tag{5.17}$$

The distribution of the parameter $\delta = \frac{d_f}{C_{in}}$ is shown in figure 5.7. The average $\bar{\delta} =< \frac{d_f}{C_{in}} >$ is shown as a dashed line. Cases S1 and S2 are excluded from the analysis due to the very short duration of their inertial phase (see table 2.2).

The average non-dimensional parameter is estimated as $\bar{\delta} = (0.29 \pm 0.04)$ at the 95% confidence level. Expressing $d_f = \bar{\delta} C_{in}$, equation (5.12) is obtained as

$$r(t) = \kappa (C_{in})^{1/4} t^{\frac{3}{4}} \tag{5.18}$$

where $\kappa = \kappa_s \bar{\delta} = (0.7 \pm 0.1)$. Despite the size of the error, the estimate is in good agreement with the value provided in the literature [Britter, 1979, Huppert, 1982] for the asymptotic spreading, i.e.

$$k = (0.84 \pm 0.06). \tag{5.19}$$

A similar estimate for the parameter κ can be obtained by directly using the scaling factor (5.17) in the plot of $r/(C_{in} t^{3/4})$ vs. t/t_i and proceeding

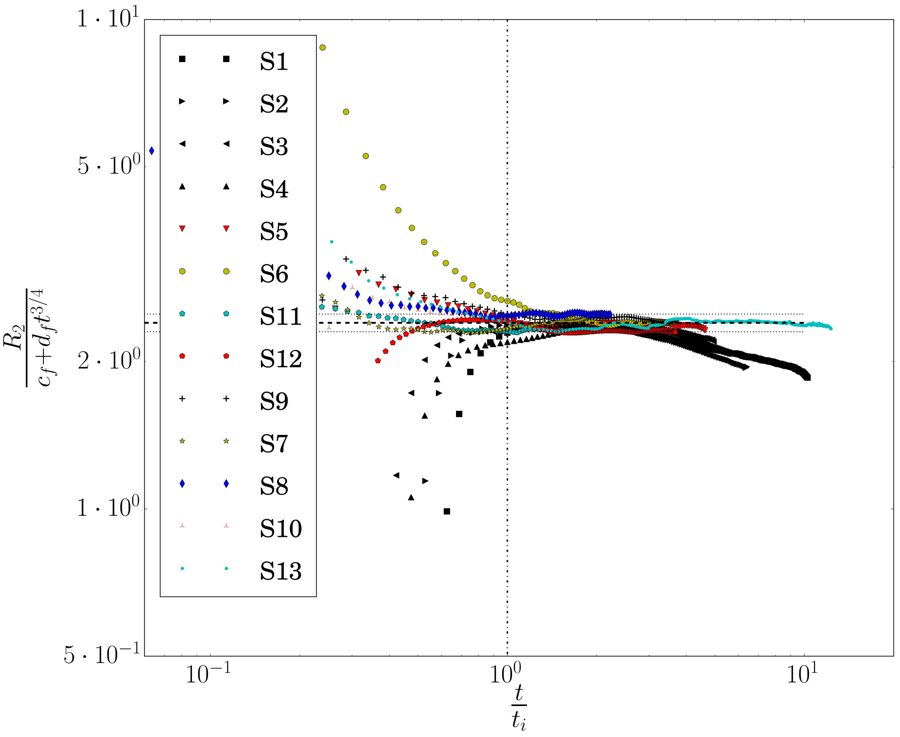

Figure 5.6: Domain of existence of the inertial-buoyancy regime (5.12): non-dimensional radius vs. non-dimensional time. Dashed line indicates $R/(c_f + d_f t^{3/4}) = \kappa_s$; dotted lines indicate the interval at the 95 % confidence level. Vertical dash-dot line indicates the theoretical transition to the inertial regime

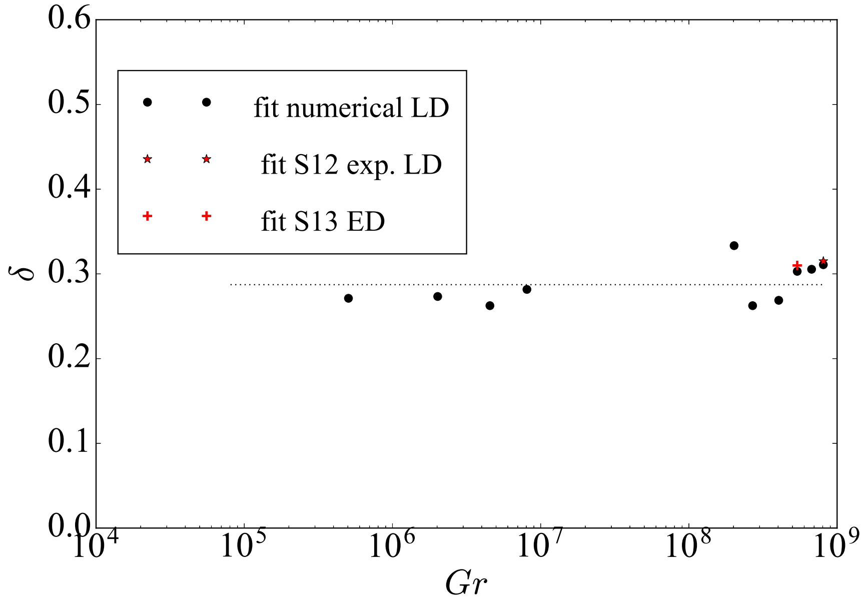

Figure 5.7: Non-dimensional coefficient $\delta = \frac{d_f}{C_{in}}$ in (5.12) vs. Gr, cases S3–S12. Dashed line represents $\bar{\delta} =< \frac{d_f}{C_{in}} >$

as in figure 5.6. In this case, the interval of values of κ can be read directly from figure 5.8. The most obvious difference with respect to figure 5.6 is that a clear dependence of κ from Gr is now observed. At least three different levels of κ are detectable, i.e. $\kappa_1 = 0.6$ for case S1, $\kappa_2 = 0.65$ for cases S2–S5 and $\kappa_3 = 0.7$ for cases S6–S13. Since κ cannot depend on the viscosity, the splitting in a band of values $\kappa_1, \kappa_2, \kappa_3$ must have been introduced by the use of the flow rate Q in the non-dimensionalization procedure. In fact, the assumption implicitly made here and above is that the entire inflow Q is the source of the axisymmetric current at the axis position. However, this assumption is not consistent with the kinematics of the flow described in Chapter 3, where it is shown that the inflow Q is split in a radial flow with the vertical axis $(x_c(t), z_0)$ moving on the horizontal plane and a longitudinal flow that slowly translates the entire radial current along the x axis.

Assuming that the estimate (5.19) holds for axisymmetric constant-flow-rate gravity currents, it is possible to assess the flow rate at the moving symmetry axis indirectly from the differences between κ_i, $i = 1, 2, 3$, and k in the following way. The simplest assumption reflecting the kinematics of the problem is then to take $Q = q + q'$, where q is the radial part of the flow and q' is the translating part. In this case,

$$\frac{r}{([q+q']g')^{1/4}\, t^{3/4}} = \frac{r}{(qg')^{1/4}\, t^{3/4}[1+\xi]^{1/4}} \tag{5.20}$$

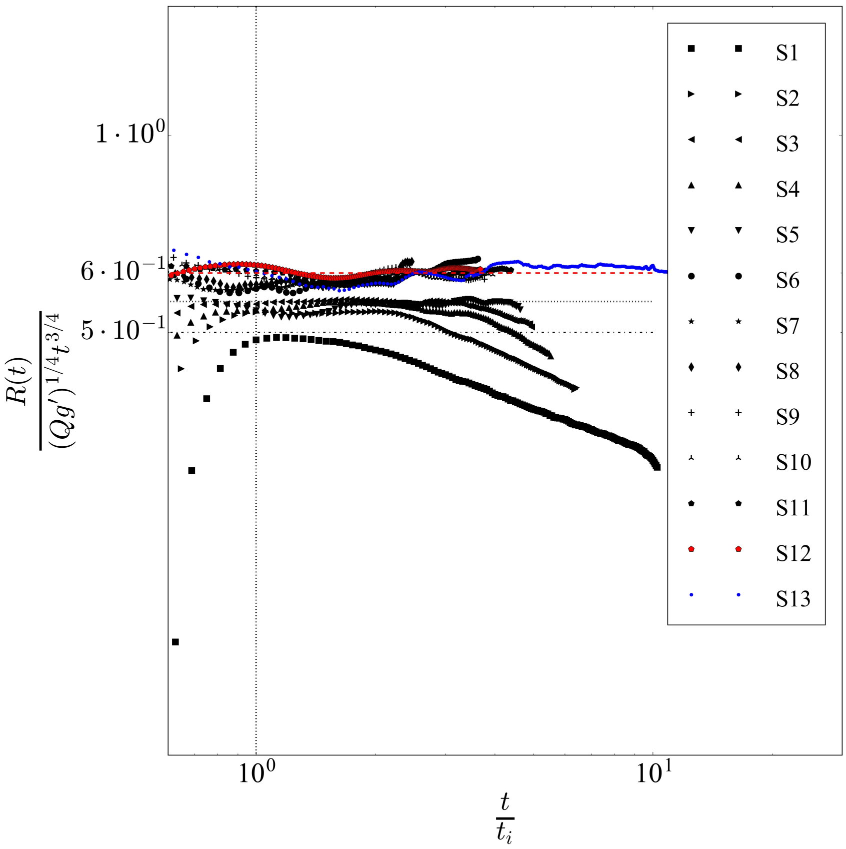

Figure 5.8: Inertial buoyancy regime (5.6): non-dimensional radius vs. non-dimensional time scaled as in [Britter, 1979]. Dashed red line indicates $R/(C_{in}t^{3/4}) = \kappa_1$; dotted line indicates $R/(C_{in}t^{3/4}) = \kappa_2$. Dot-dashed line indicates $R/(C_{in}t^{3/4}) = \kappa_3$. Vertical dash-dot line indicates the theoretical transition to the inertial regime; Q is assumed as the flow rate in the axial position

where $\xi = \frac{q'}{q}$. If the estimate (5.19) is correct, then $\frac{r}{(qg')^{1/4}t^{3/4}} = \kappa = 0.84$. A simple expansion in (infinite) series of $[1+\xi]^{-1/4} = [1-\frac{1}{4}\xi+\frac{5}{32}\xi^2-\frac{45}{384}\xi^3+...]$ yields

$$(1 - \frac{1}{4}\xi + \frac{5}{32}\xi^2 - ...) = \frac{\kappa_i}{\kappa} \tag{5.21}$$

for i=1,2,3. Then, a raw first-order estimate would be

$$-\frac{1}{4}\xi + \frac{\kappa_i}{\kappa} = 0 \tag{5.22}$$

This result implies that for very low Grashof numbers (i.e. S1 and κ_1), $\frac{q'}{q} \sim 1.2$, and the radial inflow q is less than the translating flow q' along x. For intermediate Gr (i.e. S2–S4 and κ_2), $\frac{q'}{q} \sim 0.9$, i.e. the radial inflow is slightly larger than the translating flow. Finally, for high Gr (S6–S12 and κ_3), $\frac{q'}{q} \sim 0.7$, and the radial inflow is larger than the translating flow.

5.5 Viscous-buoyancy equilibrium phase

As predicted from the transition times t_v in table 2.2, a viscous-buoyancy phase corresponding to the asymptotic law (5.7) is found only for the low Grashof number cases, i.e. from S1 to S4. In the four cases studied, the value of the Pearson correlation coefficient is above $\mathcal{R}^2 = 0.998$ for the least squares fit to (5.13). In the other cases, the external front of the gravity current hits the lateral boundary before or just after entering the viscous-buoyancy regime. The buoyancy-viscous regime is visible in figure 5.9 after the transition time $t/\ t_v = 1$, where, as indicated by the horizontal dashed line, $\frac{R_3}{e_f+g_f\sqrt{t}} = 1$. Because e_f is small, to relate the expression found (5.13) to the asymptotic law (5.7), it is necessary to express the empirical coefficient g_f in terms of C_{vis}, where

$$C_{vis} = \left(\frac{g'Q^3}{\nu}\right)^{1/8} \tag{5.23}$$

The relation must hold in all cases considered. It is found by considering the distribution of non-dimensional ratios $\lambda = \frac{g_f}{C_{vis}}$, as shown in figure 5.10.

The average ratio $\bar{\lambda} =< \frac{g_f}{C_{vis}} >= (0.75 \pm 0.07)$ is also shown as a dashed line. The error is taken as the 95% confidence interval based on the standard deviation of the individual ratios from the mean. The expression (5.7) then becomes

$$r(t) = \bar{\lambda} C_{vis}\sqrt{t} \tag{5.24}$$

Note that even in the longest time series available, S1, the current remains in the viscous-buoyancy regime for less than the corresponding $t_f - t_v$, which is a short time to correctly represent the asymptotic viscous regime. In

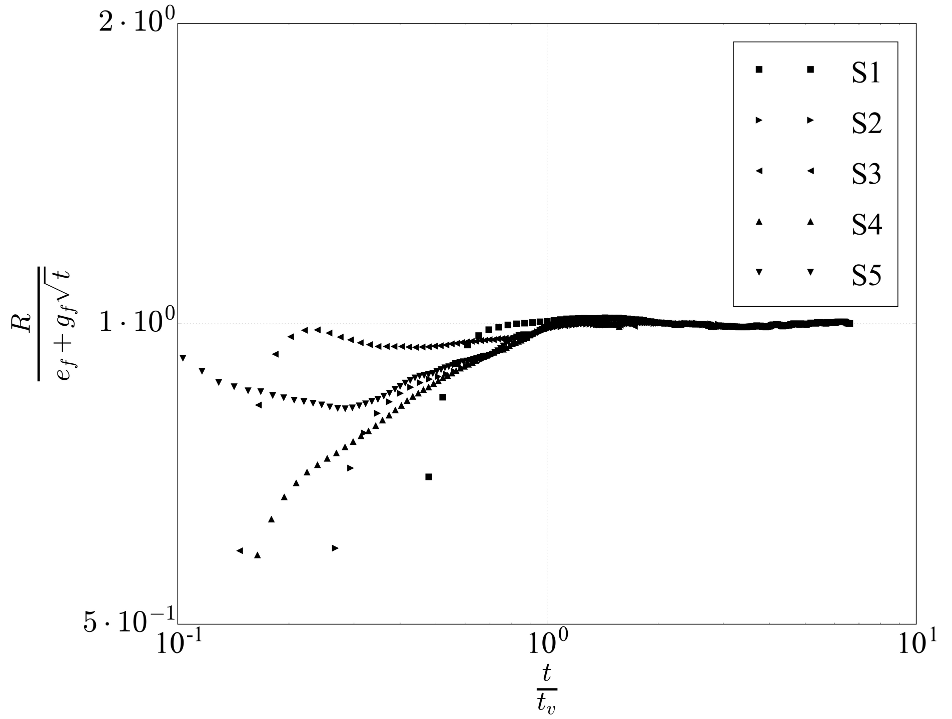

Figure 5.9: Temporal domain of existence of the viscous-buoyancy regime (5.13): non-dimensional radial position vs. non-dimensional time. Dotted line indicates $\frac{R_3}{e_f+g_f\sqrt{t}} = 1$.

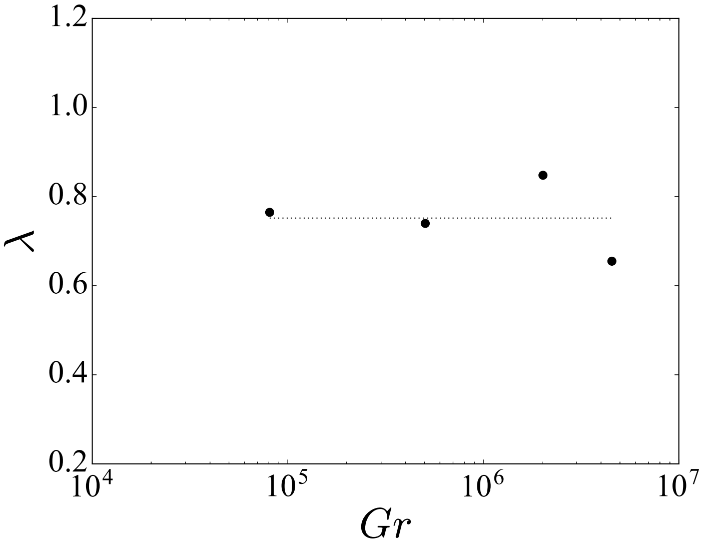

Figure 5.10: Distribution of the non-dimensional coefficient λ in the fit (5.13) vs. Gr, cases S1–S4. Dotted line represents $\bar{\lambda} =< \frac{g_f}{C_{vis}} >$

comparison, the experiments of Didden and Maxworthy [1982], which were conducted in the same range of ϵ but with flow rates at least six times smaller than that used in the present study, lasted for more than twenty minutes. Moreover, note that in the final part of the simulation, the flow is close to the wall; thus, the conditions are somewhat different from the case in which the current spreads without the presence of walls. All factors account for the small difference with respect to the value referenced in the literature, which is (0.60±0.02) [see Britter, 1979, Didden and Maxworthy, 1982, Huppert, 1982].

Part III

Conclusions

A series of large eddy simulations of three-dimensional lock-exchange gravity currents have been conducted in the set up described in [La Rocca et al., 2008, 2012, Lombardi et al., 2017] with $d/2z_0 <= 0.1$ for a wide range of Grashof numbers, from $Gr = 10^4$ to almost $Gr = 10^9$. In all cases considered, upon removal of the gate, an initial transient develops, in which the flow rate increases up to an asymptotic value. Subsequently, the dimension of the lock volume is large enough to maintain a steady flow rate Q during the evolution of the gravity current.

The flow becomes axially symmetric soon after the formation of the current, while the inflow rate at the gate remains reasonably constant throughout all the simulations. The frontline shape of the gravity current maintains a circular form, with the centre of the circle translating along x and the radius increasing monotonically in time. The axisymmetric current behaves as being driven by a virtual source at $(x_0(t),\ z_0)$ slowly moving in time along the mid-section of the tank. As predicted by Bonnecaze et al. [1995], Grundy and Rottman [1986] the flow is characterised by the presence of hydraulic shocks. The analysis of velocity and density fields indicates the presence of rings as periodic perturbations of the dense flow at sufficiently high Gr, i.e. for $Gr \geq 2.7 \cdot 10^8$. Isolated shocks are detectable in the range $5 \cdot 10^5 \leq Gr \leq 2 \cdot 10^8$. In the latter case the structure of the current, characterised by the head of the current being constrained between a forward and a rear shocks is consistent with the model of Garvine [1984].

Shocks are associated to internal circular jumps [Thorpe and Kavcic, 2008] which are not stationary. The high velocity structures, present on the supercritical side of the jump are associated with Kelvin-Helmholtz billows. The combined action of hydraulic jumps in the internal core of the current and the mixing action of the Kelvin-Helmholts instabilities at the top of the current is responsible for the growth of the structures visible in the density fields.

When rings are continuously formed, the number of rings generated in a fixed time period is a monotonic function of the flow rate, consequently the dimensionless frequency of ring generation η is nearly independent of Gr. The estimated value is $\bar{\eta} = 0.48 \pm 0.06$. In the initial stage of development of the flow the rings are generated in the flow region where the frontline was in the inertial regime, and move through the entire body of the current. In some cases they are able to interact with the external front. As the radial spreading of the current exceeds a critical radial distance, most of the rings, which continue to be generated, remain confined inside a circular sector, while the frontal structure continues to advance regularly. Only a few shocks are able to escape and move through the current up to the external frontline.

Considering the purely axial symmetric part of the gravity current, three distinct spreading regimes are found: slumping, inertial and viscous. These regimes are quite similar in nature to those studied in the case of constant-volume axisymmetric gravity current but follow the characteristic scaling laws for constant-flow-rate sources. An analytical expression for the slumping, which is derived from an extension of the box model of Huppert and Simpson [1980] to the case of a constant inflow axisymmetric current, is found to fit the initial part of the spreading in all cases. The slumping phase starts just before or right at the time t_0 for which the flow rate at the gate, Q, stabilises. The duration of the slumping depends on the buoyancy acceleration at the gate, and the non-dimensional duration is a linear function of the Froude number at the gate. However, it is extremely short at very small Grashof numbers. The radial expansion in time given by the slumping model, $r \propto t^{7/8}$, is similar to the 'spreading' law $r \propto t^{0.92}$ proposed analytically by Garvine [1984]. The present results help to clarify the controversial theoretical results found for the initial spread of the gravity current by Garvine [1984] and Chen [1980]: the former, proceeding forward in time in the solution of the initial value problem, found a 'spreading' phase before a hydraulic jump region ('a trailing front'), whereas the latter, proceeding backward in solving the similarity differential equation, hit the discontinuity while still in the inertial range. In other words, they may have fallen in different 'initial' asymptotical regimes.

The presence of an inertial regime following the asymptotic law (5.6) is verified in all cases. The expression found, $r(t) = 0.7(C_{in})^{1/4}t^{\frac{3}{4}}$, is consistent with the elementary scaling laws of Chen [1980] and the results from the laboratory experiments of Britter [1979]. The confidence interval obtained here for the numerical coefficient in the expression is larger than that obtained by Britter [1979] due to the use of the flow rate at the gate, Q, in the parameter C_{in} rather than the true inflow source at the symmetry axis $(x_c(t), z_0)$.

The viscous-buoyancy regime, as predicted by Huppert [1982], is also detected in the cases with lower Grashof numbers, with the front propagation expressed as $r(t) = \bar{\lambda} C_{vis}\sqrt{t}$. The agreement with the theory is satisfactory given that only a fraction of the viscous-buoyancy regime could be simulated in the present domain.

The research shows that when the geometric condition on the gate $\frac{d}{2y_0} < \frac{1}{10}$ is satisfied, three-dimensional unconstrained gravity currents generated by lock exchange evolve rapidly in axial symmetric, constant inflow gravity currents. This imply that, provided the width of an estuary or river mouth is sufficiently small, the near field of dispersion of a buoyant riverine plume has a dynamics which is not different from the dynamics of a volcanic base surge or of a constant inflow point source oil spill. The same applies to mesoscale density driven processes like downdrafts in thunderstorms. It is not of secondary importance that all such complex flows can be studied using lock exchange rather using more elaborate techniques. An important point to be further investigated, possibly by using simulations at even higher resolution, would be the analysis of the averaged and turbulent kinetic energies for the decomposed axisymmetric and planar velocity field. The presence of characteristic shocks, which are continuously generated if the nondimensional volume flux is sufficiently high, suggests the process of mixing for axial symmetric, constant inflow gravity currents to be significatively different from that expected for plane gravity currents. This investigation would be an important perspective for future work in the field.

Acknowledgements

The laboratory experiment S12 was carried out by dr. Valentina Lombardi of Roma Tre University as a part of an extensive laboratory research project on 3D gravity currents. The post-processed results of the experiment have been kindly provided to the author of this thesis with extensive support information (pictures, movies and practical demonstrations).

The original LES-COAST code has been provided by Prof. Vincenzo Armenio (University of Trieste), the original code for pre-processing has been kindly provided by dr. Federico Roman (University of Trieste).

The preliminary study on the problem geometry and the implementation of the LES model for the 3D gravity current problem was carried out by dr. Luisa Ottolenghi.

This study could not have been carried out without the constant assistance of dr. Valentina Lombardi (University of Roma Tre), dr. Federico Roman (University of Trieste), Prof. Vincenzo Armenio (University of Trieste) and, of course, Prof. Claudia Adduce (University of Roma Tre).

The author acknowledges PRACE for awarding access to resources MareNostrum based in Spain at the Barcelona Supercomputing Centre, to Galileo in Italy at Cineca. The support of John Donners from SurfSara, Netherlands, for the technical work is gratefully acknowledged.

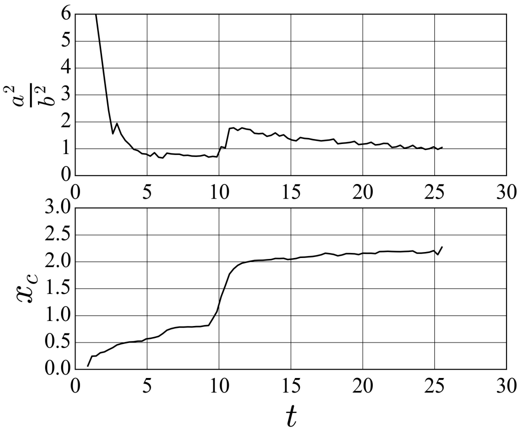

Figure A1: Case S5: $Gr = 8.1 \cdot 10^6$, $\epsilon = 0.03$; top panel $\frac{a^2}{b^2}$ vs. t; bottom panel $x_c(t)$ vs. t

Appendix A

As mentioned in Chapter 3, in the absence of disturbances, it is easy to identify the two extrema of the frontline $G(x, y)$ by considering the maximum of the function $y_+ = f_l(x)$ above and the minimum y_- of the function below the symmetry axis of the gravity current. If $G(x, y)$ is an ellipse (or a circle), then the two points have the same projection on the x axis, x_c. When lobes and clefts are present on the frontline, it is clear that the position of the extrema of $f_l(x)$ might not correspond to the correct position x_c. The geometry of the problem can be described using three distances: a, b and R_c. b is evaluated as half the distance between the two extremal points $b = 0.5(y_+ - y_-)$. a is obtained from the distance between the frontline position on the x axis, x_f, and the x-coordinate of the symmetry axis x_c, i.e. $a = x_f - x_c$. A third length is the distance between the fixed point at the centre of the gate x_0 and x_f, i.e. $R_c = x_f - x_0$. To visualise how the determination of the frontal spreading is affected by the presence of lobes ad clefts, the frontline is analysed before and after $t = 10$ in Figure A1, case S5. The frontline $G(x, y)$ at time $t = 9.3$ is plotted in figure A2a as a series of black dots. Three different circles are superimposed: the black continuous circle, C_f, is centred at the fixed centre of the gate (x_0, y_0) and has radius R_c. The red dotted-dashed circle C_b is centred at the moving point (x_c, y_0) and has radius $R_b = b$. The blue dashed circle C_a is centred at the moving point (x_c, y_0) and has radius $R_a = a$. Due to the presence of lobes and clefts, the extrema of the frontline, y_+ and y_-, indicated by small red crosses, are found symmetrically on a large lobe in the rear part of the frontline. Consequently, C_b is behind C_f, and the value of x_c lags with

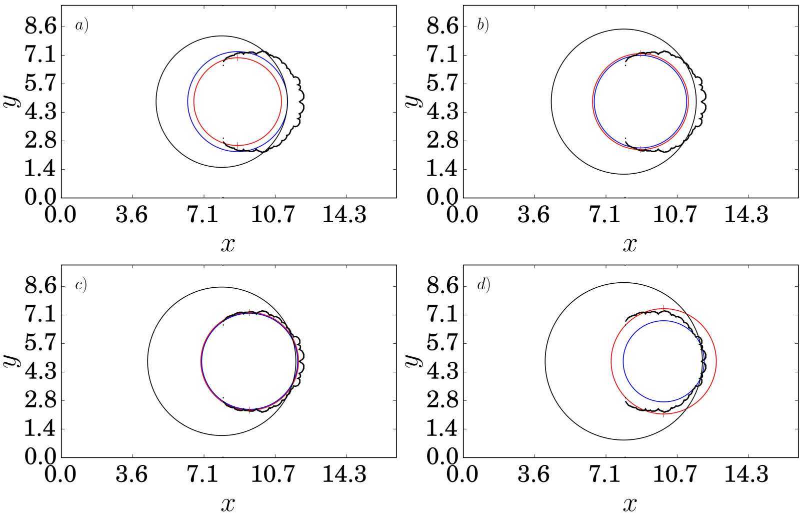

Figure A2: Case S5 a) t=9.3, b) t=9.8, c) t=10.1, and d) t= 10.5; frontline $G(x, y)$ is indicated with black dots; C_a: blue dashed circle; C_b: red dot-dashed circle; C_f: black solid circle; y_+ and y_- are indicated with red crosses

respect to the true centre of the frontline. Meanwhile, x_c being small and underestimated causes a to be overestimated, compensating the error in C_a. The extremum y_+ remains blocked on the same lobe, and in time, the C_b lags progressively back. This continues until the error in the position of x_c cannot be compensated by the overestimation of a, and both circles C_a and C_b are found behind C_f at t=9.8 (figure A2b). At t=10.1, the lobes and clefts in the rear of the frontline smooth out (figure A2c). Consequently, y_+ and y_- indicate again the real position of the frontline centre x_c. All circles in figure A2c intersect the frontline at the same point on the x axis. It is evident that both C_a and C_b closely follow most of the frontline, whereas C_f is close to the frontline only near the x axis. This instant is the time when $\frac{a^2}{b^2} = 1$ and $x_c(t)$ jumps from 1 to almost 2 in figure A1.

At the subsequent time t=10.5, a new lobe emerges in the leading part of the frontline. The reverse process occurs now: the value of x_c becomes overestimated, and C_b starts to lead with respect to C_f (figure A2d). With x_c being overestimated, R_a becomes smaller than R_b and R_c, and some compensation of the error again occurs at t=11. Towards the end of the numerical simulation, the influence of the lobes and clefts on the form of the frontline becomes small, the three circles almost intersect on the x axis, and the situation is similar to the one shown for t=10.1.

Since the typical life span of the individual lobes is small compared to the duration of any simulation or experiment, a correction for the estimate of the radius of the circular frontline and the position x_c of the centre along the x axis can be implemented. The method proposed herein is based on the comparison of the two distances a and b at each time.

Case 1) $R_b > R_a$, C_b leads, indicating that x_c is too advanced (figure A2d). In this case, a secondary relative maximum is searched for to the left-hand side of the frontline and R_b, R_a and x_c are re-evaluated. This step is repeated until the difference $R_b - R_a$ falls under a given small threshold or until the difference changes sign. In the first case, if R_a and R_b are also close to R_c, then they are a good estimate of the real radius, and the 'correct' position of $x_c(t)$ and the radius R_a are stored. If the difference changes sign, it means that C_b now lags, and x_c is at the rear of the true centre. In this case, if the absolute value of the difference is small, x_c and R_a are stored. Otherwise, a position (not necessarily a relative maximum) in the reverse direction is searched for until the absolute difference $|R_b - R_a|$ becomes sufficiently small. The last situation is found to seldom occur, particularly when very large lobes exist and the frontline remains relatively flat due to the presence of smaller lobes ahead. Case 2) $R_a > R_b$, the situation is reversed and the method works in the same manner with opposite signs.

Appendix B

In the original box model formulation of Huppert and Simpson [1980], which accounts for both the slumping and the inertial-buoyancy regimes, the initial geometry is a circular cylinder of dense fluid with height H and radius R_0 separated from a less dense ambient fluid by a removable wall. At the beginning of the simulation, all the walls that bound the dense fluid are removed, and the current expands in the radial direction. The analytical expression for the front position in time is based on the assumption that the volume of the gravity current does not change in time and that the velocity of the front in terms of the Froude number at the head of the current $Fr = \frac{\dot{R}}{\sqrt{g'h}}$ depends only on the ratio $\phi = \frac{h}{H}$, based on Britter [1979], as

$$Fr = \begin{cases} \frac{1}{2}\phi^{-1/3}, & 0.075 < \phi < 1. \\ const. = 1.19, & \phi < 0.075. \end{cases} \tag{25}$$

The first case is observed when the current depth is still comparable with the total depth of the fluid, and the second is valid when the current has a depth that is considerably smaller than the total depth of the fluid [see also Marino et al., 2005]. It is relatively straightforward to derive a 'slumping box model' with the constant-flow-rate assumption in place of the hypothesis of constant flow volume. Indeed, assuming that the initial current is close to axisymmetric, the assumption $Qt = \pi r^2 h$ may be used to obtain a first guess of h to use in

$$Fr = \frac{\dot{r}}{\sqrt{g'h}} = 1/2\left(\frac{H}{h}\right)^{1/3} \tag{26}$$

i.e.

$$\dot{r} = \frac{1}{2}\left((g'h)^3\left(\frac{H}{h}\right)^2\right)^{1/6} = \frac{1}{2}\left(2g'^3\frac{qt}{\pi r^2}H^2\right)^{1/6}. \tag{27}$$

Separating the variables r and t, the differential equation is easily solved by separating variables, after which

$$r^{4/3} - r_0^{4/3} = \frac{4}{7}\left(\frac{g'^3 q H^2}{\pi}\right)^{1/6} t^{7/6} \tag{28}$$

or equivalently,

$$\left(\frac{r}{r_0}\right)^{4/3} = 1 + \frac{4}{7}\left(\frac{g'^3 q H^2}{\pi r_0}\right)^{1/6}\left(\frac{t}{r_0}\right)^{7/6} \tag{29}$$

when $t \gg \frac{r_0}{\left(\frac{g'^3 q H^2}{\pi r_0}\right)^{1/7}}$

$$r(t) = \left(\frac{4}{7}\right)^{3/4}\left(\frac{g'^3 q H^2}{\pi}\right)^{1/8} t^{7/8}, \tag{30}$$

which is incidentally not far from the expression found by Garvine [1984].

To evaluate the transition time t_i when the Fr number becomes constant, when $t \to t_i$, $\phi \to \phi_0 = 0.075 = h/H = \frac{Qt_i}{\pi r_s^2 H}$, such that $r_s{}^2 = r_0{}^2 + \frac{Qt_i}{\pi\phi_0 H}$ and

$$\left[r_0{}^2 + \frac{Qt_i}{\pi\phi_0 H}\right]^{2/3} - r_0{}^{4/3} = \frac{4}{7} C_{sl}^{1/6} t^{7/6} \tag{31}$$

i.e.

$$\left(\frac{Qt_i}{\pi\phi_0 r_0{}^2 H}\right)^{2/3} \left[1 + \frac{\pi\phi_0 r_0{}^2 H}{Qt_i}\right]^{2/3} - r_0{}^{4/3} = \frac{4}{7} C_{sl}^{1/6} t_i^{7/6}. \tag{32}$$

since $\left(2/3 \frac{\pi\phi_0 H}{Qt_i}\right)^{5/3} \gg r_0{}^{2/3}$

$$\left(\frac{Qt_i}{\pi\phi_0 H}\right)^{2/3} = \frac{4}{7} C_{sl}^{1/6} t_i^{7/6} \tag{33}$$

hence,

$$t_i^{1/2} = 7/4 (\frac{Q}{\pi\phi_0 H})^{1/2} \frac{\pi}{Qg'^3 H^2} \tag{34}$$

or,

$$t_i = (\frac{7}{4\phi_0^{2/3}})^2 \frac{Q}{\pi g' H^2} \tag{35}$$

Bibliography

Abbott, M. B. and Hayashi, T. (1967). Unsteady radial flow of oil being discharged from a source in the ocean. *Proc. Coastal Eng. Conf. Jap. Soc. Civil Eng. (14th), Tokyo*, pages 228–229.

Adduce, C., Sciortino, G., and Proietti, S. (2012). Gravity currents produced by lock exchanges: Experiments and simulations with a two-layer shallow-water model with entrainment. *J. Hydraul. Eng.-ASCE*, 138(2):111–121.

Armenio, V. and Piomelli, U. (2000). A lagrangian mixed subgrid-scale model in generalized coordinates. *Flow Turbul. and Combust.*, 65(1):51–81.

Armenio, V. and Sarkar, S. (2002). An investigation of stably stratified turbulent channel flow using large-eddy simulation. *J. Fluid Mech.*, 459:1–42.

Bhattacharjee, J. K. and Ray, A. K. (2011). Hydraulic jump. *Journal of Physics: Conference Series*, 319(doi:10.1088/1742-6596/230/1/012046).

Bohr, T., Dimon, P., and Putkaradze, V. (1993). Shallow-water approach to the circular hydraulic jump. *Journal of Fluid Mechanics*, 254:635–648.

Bonnecaze, R. T., Hallworth, M. A., Huppert, H. E., and Lister, J. R. (1995). Axisymmetric particle-driven gravity currents. *J. Fluid Mech.*, 294:93–121.

Britter, R. (1979). The spread of a negatively buoyant plume in a calm environment. *Atmospheric Environment*, 13:1241–1247.

Cantero, M., Lee, J., Balachandar, S., and Garcia, M. (2007). On the front velocity of gravity currents. *J. Fluid Mech.*, 586:1–39.

Chen, J. C. (1980). Studies on gravitational spreading currents. *PhD Thesis, California Institute of Technology.*

Cuthbertson, A. J. S., Laanearu, J., Wåhlin, A. K., and Davies, P. (2011). Experimental and analytical investigation of dense gravity currents in a rotating, up-sloping and converging channel. *Dynamics of Atmospheres and Oceans*, 52(3):386–409.

Cuthbertson, A. J. S., Lundberg, P., Davies, P. A., and Laanearu, J. (2014). Gravity currents in rotating, wedge-shaped, adverse channels. *Environ. Fluid Mech.*, 14(5):1251–1273.

Dai, A. (2013). Experiments on gravity currents propagating on different bottom slopes. *J. Fluid Mech.*, 731:117–141.

Dai, A. (2015). High-resolution simulations of downslope gravity currents in the acceleration phase. *Phys. Fluids*, 27(7):076602.

Dai, A. and Wu, C.-S. (2016). High-resolution simulations of cylindrical gravity currents in a rotating system. *J. Fluid Mech.*, 806:71–101.

Didden, N. and Maxworthy, T. (1982). The viscous spreading of plane and axisymmetric gravity currents. *J. Fluid Mech.*, 121:27–42.

Fay, J. A. (1969). *The Spread of Oil Slicks on a Calm Sea*, volume Oil on the Sea: Proceedings of a symposium on the scientific and engineering aspects of oil pollution of the sea, sponsored by Massachusetts Institute of Technology and Woods Hole Oceanographic Institution and held at Cambridge, Massachusetts, May 16, 1969 of *isbn=978-1-4684-9019-0.* Springer US.

Garvine, R. W. (1984). Radial spreading of buoyant, surface plumes in coastal waters. *Journal of Geophysical Research*, 89(C2):1989–1996.

Gonzalez-Juez, E., Meiburg, E., Tokyay, T., and Constantinescu, G. (2010). Gravity current flow past a circular cylinder: forces, wall shear stresses and implications for scour. *J. Fluid Mech.*, 649:69–102.

Gratton, J. and Vigo, C. (1994). Self-similar gravity currents with variable inflow revisited: plane currents. *J. Fluid Mech.*, 258:77–104.

Green, T. I. and Ragotzkie, R. A. (1972-1973). Application of remote sensing to the investigation of nearshore mixing and coastal entrapment in large ater bodies. A progress report on multidisciplinary research on the application of remote sensing to water resources problems NASA-CR136280, NASA.

Grundy, R. and Rottman, J. W. (1986). Self-similar solutions of the shallow-water equations representing gravity currents with variable inflow. *J. Fluid Mech.*, 169:337–351.

Hallworth, M. A., Huppert, H. E., and Ungarish, M. (2001). Axisymmetric gravity currents in a rotating system: experimental and numerical investigations. *J. Fluid Mech.*, 447:1–29.

Härtel, C., Meiburg, E., and Necker, F. (2000). Analysis and direct numerical simulation of the flow at a gravity-current head. part 1. flow topology and front speed for slip and no-slip boundaries. *J. Fluid Mech.*, 418:189–212.

Hoult, D. P. (1972). Oil spreading on the sea. *Ann. Rev. Fluid Mech.*, 4:341–368.

Huppert, H. (1982). The propagation of two-dimensional and axisymmetric viscous gravity currents over a rigid horizontal surface. *J. Fluid Mech.*, 121:43–58.

Huppert, H. E. (2006). Gravity currents: a personal perspective. *J. Fluid Mech.*, 554:299–322.

Huppert, H. E. and Simpson, J. E. (1980). The slumping of gravity currents. *J. Fluid Mech.*, 99(04):785–799.

La Rocca, M., Adduce, C., Sciortino, G., and Pinzon, A. B. (2008). Experimental and numerical simulation of three-dimensional gravity currents on smooth and rough bottom. *Phys. Fluids*, 20(10):106603.

La Rocca, M., Adduce, C., Sciortino, G., Pinzon, A. B., and Boniforti, M. A. (2012). A two-layer, shallow-water model for 3d gravity currents. *J. Hydraul. Res.*, 50(2):208–217.

Lombardi, V., Adduce, C., and La Rocca, M. (2017). Unconfined lock-exchange gravity currents with variable lock width: laboratory experiments and shallow-water simulations. *Journal of Hydraulic Research*, in press.

Lombardi, V., Adduce, C., Sciortino, G., and Rocca, M. L. (2015). Gravity currents flowing upslope:laboratory experiments and shallow water simulations. *Phys. Fluids*, 27(1):016602.

Marino, B. M., Thomas, L. P., and Linden, P. F. (2005). The front condition for gravity currents. *J. Fluid Mech.*, 536:49–78.

Maxworthy, T. (1980). On the formation of nonlinear internal waves from the gravitational collapse of mixed regions in two and three dimensions. *J. Fluid Mech.*, 96:47–64.

Meiburg, E., Radhakrishnan, S., and Nasr-Azadani, M. (2015). Modeling gravity and turbidity currents: Computational approaches and challenges. *Applied Mechanics Reviews*, 67(4):040802–22.

Meneveau, C., Lund, T., and Cabot, W. (1996). A lagrangian dynamic subgrid-scale model of turbulence. *J. Fluid Mech.*, 319:353–385.

Ooi, S., Constantinescu, G., and Weber, L. (2007). 2d large-eddy simulation of lock-exchange gravity current flows at high grashof numbers. *J. Hydraul Eng.-ASCE*, 133:1037–1047.

Ooi, S., Constantinescu, G., and Weber, L. (2009). Numerical simulations of lock-exchange compositional gravity current. *J. Fluid Mech.*, 635:361–388.

Ottolenghi, L., Adduce, C., Inghilesi, R., Armenio, V., and Roman, F. (2016a). Entrainment and mixing in unsteady gravity currents. *Journal of Hydraulic Research*, 54(5):541–557.

Ottolenghi, L., Adduce, C., Inghilesi, R., Roman, F., and Armenio, V. (2016b). Mixing in lock-release gravity currents propagating up a slope. *Physics of Fluids*, 28(doi: 10.1063/1.4948760):056604.

Ottolenghi, L., Adduce, C., Roman, F., and Armenio, V. (2017). Analysis of the flow in gravity currents propagating up a slope. *Ocean Modelling*, 115:11–13.

Patterson, M., Simpson, J., Dalziel, S., and van Heijst, G. (2004). The development of an axisymmetric gravity current. *Mechanics of 21st Century - ICTAM04 Proceedings.*

Penney, W. G. and Thornhill, C. K. (1952). Part iii. the dispersion, under gravity, of a column of fluid supprted on a rigid horizontal plane in some gravity wave problems in the motion of perfect liquids. *Philosophical Transactions of the Royal Society of London*, 244A:285–311.

Piomelli, U. and Balaras, E. (2002). Wall-layer models for large-eddy simulations. *Annu. Rev. Fluid Mech.*, 34:349–74.

Piomelli, U. and Chasnov, J. R. (1996). *Large-Eddy Simulations: Theory and Applications*, pages 269–336. Springer Netherlands, Dordrecht.

Roman, F., Napoli, E., Milici, B., and Armenio, V. (2009). An improved immersed boundary method for curvilinear grids. *Computers & Fluids*, 38(8):1510–1527.

Ross, A. N., Linden, P. F., and Dalziel, S. B. (2002). A study of three-dimensional gravity currents on a uniform slope. *J. Fluid Mech.*, 453:239–261.

Salmon, R. (1998). *Lectures on Geophysical Fluid Dynamics.* Number ISBN 0-19-510808-6. Oxford University Press.

Salon, S., Armenio, V., and Crise, A. (2007). A numerical investigation of the stokes boundary layer in the turbulent regime. *J. Fluid Mech.*, 570:253–296.

Sedov, L. I. (1993). *Similarity and Dimensional Methods in Mechanics, 10th edition*, volume ISBN-13: 978-0849393082. CRC Press.

Setvak, M., Lindsey, D., Novak, P., Wang, P., Radová, M., Kerkmann, J., Grasso, L., Su, S., Rabin, R., Stastka, J., and Charvát, Z. (2010). Satellite-observed cold-ring-shaped features atop deep convective clouds. *Atmospheric Research*, 97:80–96.

Shin, J., Dalziel, S., and Linden, P. (2004). Gravity currents produced by lock exchange. *J. Fluid Mech.*, 521:1–34.

Simpson, J. E. (1997). *Gravity currents: In the environment and the laboratory.* Cambridge University Press.

Simpson, J. E. and Britter, R. (1979). The dynamics of the head of a gravity current advancing over a horizontal surface. *J. Fluid Mech.*, 94(3):477–495.

Taylor, J., Sarkar, S., and Armenio, V. (2005). Large eddy simulation of stably stratified open channel flow. *Phys. Fluids*, 17(116602).

Thorpe, S. A. and Kavcic, I. (2008). The circular internal hydraulic jump. *Journal of Fluid Mechanics*, 610:99–129.

Tokyay, T., Constantinescu, G., and Meiburg, E. (2014). Lock-exchange gravity currents with a low volume of release propagating over an array of obstacles. *J. Geophys. Research: Oceans*, 119(5):2752–2768.

Ungarish, M. (2009). *An introduction to gravity currents and intrusions.* CRC Press.

Ungarish, M. and Zemach, T. (2005). On the slumping of high reynolds number gravity currents in two-dimensional and axisymmetric configurations. *European Journal of Mechanics B/Fluids*, 24:71–90.

Vinokur, M. (1983). On one-dimensional stretching functions for finite-difference calculations. *Journal of Computational Physics*, 50(2):215–234.

Whitham, G. (1999). *Linear and Nonlinear Waves.* Number ISBN-13: in 978-0471359425. Wiley-Interscience.

Zang, Y., Street, R., and Koseff, J. (1994). A non-staggered grid, fractional step method for time-dependent incompressible navier-stokes equations in curvilinear coordinates. *J. Comput. Phys.*, 114(1):18–33.